UiT
THE ARCTIC
UNIVERSITY
OF NORWAY

Faculty of Science and Technology
Department of Physics and Technology

6-meter wavelength polarimetric inverse synthetic aperture radar mapping of the Moon

—

Torbjørn Tveito

FYS-3907: Master's thesis in physics and Education, 8-13 . . . June 2019

Abstract

Remote sensing of planetary surfaces is an effective method for gaining knowledge of the processes that shape the planetary bodies in our solar system. This is useful for uncovering the environment of the primordial solar system and to study the current state of the upper crusts of the other planets in our neighborhood. A recent 6-meter wavelength polarimetric radar map of the Moon [39] showed unexpectedly low depolarized radar returns in two regions on the lunar nearside. These two areas were a highland region between Mare Imbrium and Mare Frigoris, and the highland area surrounding the Schiller-Zucchius impact basin. These two regions showed characteristics unlike those of typical highland regions of the lunar surface. So far, there has been no readily available explanation for this observation. In this study, it is shown that the likely cause is an increased loss tangent due to chemical differences in the first few hundred meters of the lunar soil. We also show the absence of any coherent subsurface, which could be the preserved remains of an ancient basaltic plain. We do this by comparing the 6-meter polarimetric radar map to other relevant data sets: 1) surface TiO_2 and FeO abundance, 2) surface rock population, 3) radar maps of the Moon with other wavelengths, and 4) visual spectrum images of the Moon. The area near the Schiller-Zucchius basin was shown to be consistent with other areas with similar surface chemical compositions, but the region between Mare Imbrium and Mare Frigoris showed significantly lower mean power in comparison to otherwise similar regions. While we can not conclusively determine the cause, we hypothesize that the low radar return is explained by an increased concentration of iron and titanium oxides in the volume beneath the surface, potentially due to remnants of primordial lunar volcanism. The results show that long wavelength polarimetric radar measurements of the Moon are very powerful tools for studying the earliest stages of the evolution of the Moon.

Preface

I have chosen this task due to my interest in the Moon and the early solar system in general. The work has also allowed me to learn about high power large aperture radar systems, and their application to studies of planetary bodies using the inverse synthetic aperture imaging technique. The work has also resulted in a peer reviewed journal article [39], and a popular science article discussing our findings [43].

I would like to thank my advisors, Dr. Juha Vierinen and Dr. Anthony P. Doulgeris, for assistance and guidance in the science of remote sensing, planetary science and the art of writing.

I would like to thank my parents for their support, both motivational and culinary, during the process of writing this thesis, as well as their various sage advice.

I would also like to thank my brother for his free tech support and two tactile aides in lunar surface texture mapping.

Finally, I'd like to thank my co-conspirator Zoe for our off-topic discussions.

List of Figures

Contents

1

Introduction

From the beginning of human history, man has been fascinated by the Moon. Ancient religions and myths [42] have centered around the implications of a full Moon; from the myth surrounding werewolves [44] to the magical powers of herbal medicine mixed at exactly the right time in the lunar cycle.

Ancient scientists used the lunar phases to create calendars [8], and in more recent times tide tables vital for sailing ships to enter the dock at the right moment [45]. In our days, studies of the Moon allow us to gain insight in planetary formation and increase our understanding of the Solar System.

Our Moon had a violent birth according to the Giant Impact hypothesis [6]. At an early stage of the Earth's development, approximately 4.5 G.A (billion years ago), it collided with Theia, a planetary object about the size of Mars. This collision liquefied any hard surface that might have been present at the time, and ejected large amounts of molten mantel material into space. Some of this material rained down as a hailstorm of molten lava, and some was flung out of the Earth's orbit, becoming near-Earth asteroids. The remainder became a short-lived ring system that eventually gathered to become our Moon. This hypothesis is the currently accepted explanation for how the Earth-Moon system came to be.

During the period from 4.5 G.A. to 3.8 G.A. the impact rate was much higher than it is today, meaning that the upper crust of the rocky planets were constantly being gardened by impact events. This era was called the late heavy

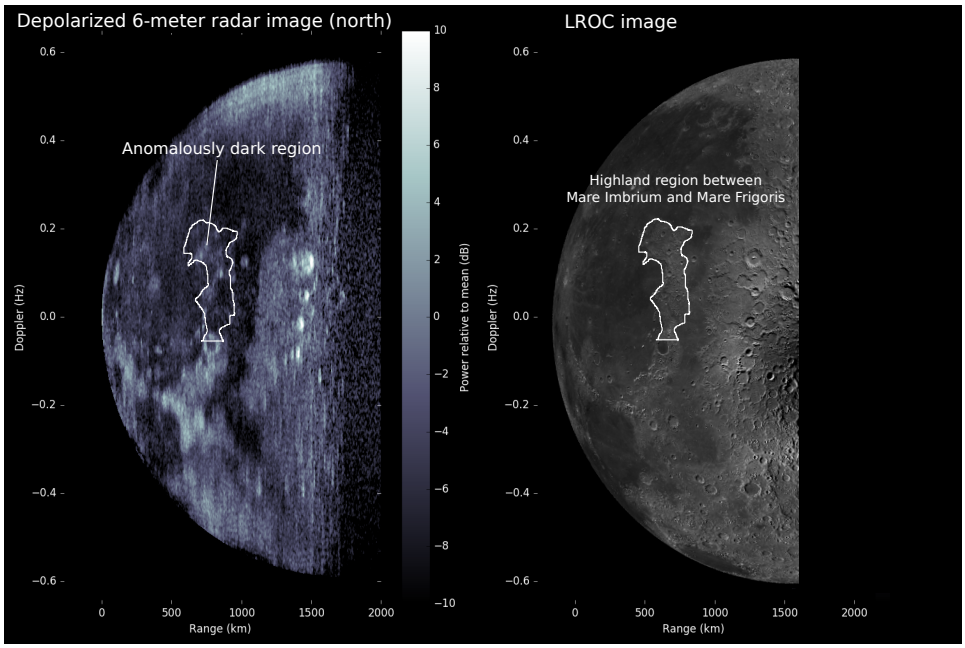

Figure 1.1: This figure shows the radar map of the northern nearside as well as an image mosaic from the Lunar Reconnaissance Orbiter Camera (LROC) database with a similar projection. The area marked shows significantly reduced depolarized power compared to other highlands nearby. Map taken from Vierinen et al. [39].

bombardment period. Approximately 3.8 billion years ago[6] the impact rate declined significantly, and structure of planetary surfaces became more stable. It is worth noting that the existence of the late heavy bombardment period is a matter of ongoing debate in the scientific community[15].

On Earth, we have an atmosphere and tectonic activity constantly reworking and reshaping the surface. Thus, we have lost much of the remnants of our Earth's primordial surfaces. These processes are absent in the lunar environment, allowing us to examine the remnants of the early development of the lunar surface. Our Moon thus resembles a time capsule, which allows us to peer further into the history of the Earth-Moon system.

The surface of the Moon can be divided into two distinct types; maria and terrae. The bright grey fields (see figures 1.1 and 1.2) are anorthositic highlands caused by the destruction of the early crustal formation in the proto-lunar magma ocean. The light anorthosites would float on top of the heavier magma as a loose layer of broken rock, growing thicker as the Moon cooled. Due to mixing and gardening by impact events, the topography of this early landscape was in constant flux. Highlands are also called terrae.

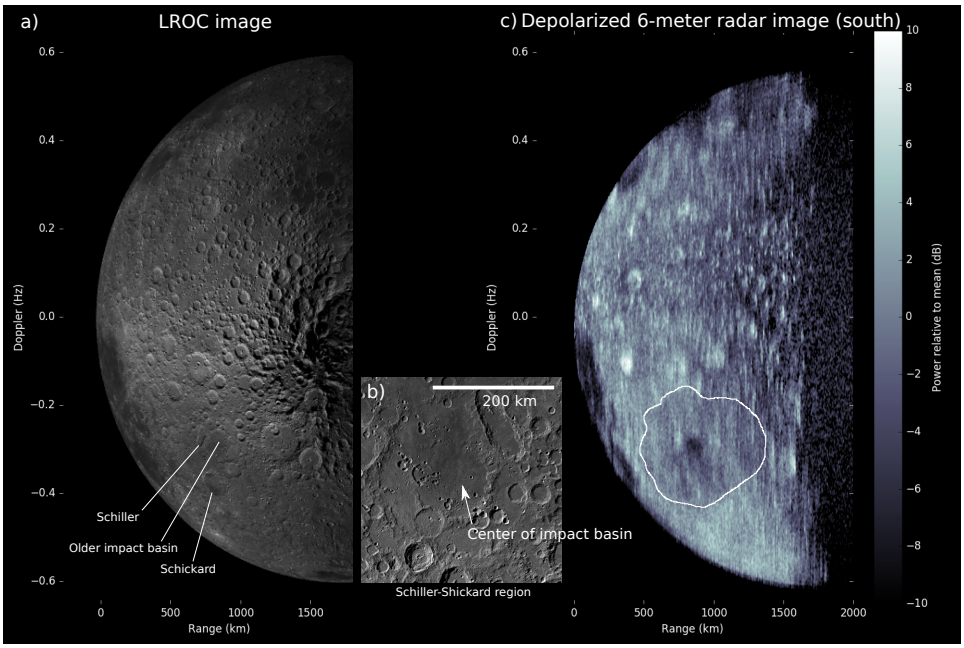

Figure 1.2: Southern nearside from the same experiment as Figure 1.1. a) shows an LROC mosaic projected around the south pole. Marked are the craters Schiller and Schickard, as well as what appears to be an ancient impact basin. b) shows a zoomed-in and rotated image of the area. c) shows the radar map, and the impact basin denoted in b) is visible here as the dark circle in the lower half of the image near 1000 km. Note the ”halo” surrounding it with a reduced power, marked with a white line.

The dark basaltic areas are volcanic flow complexes caused by later upwellings of magma after the decline of the impact rate. The frozen magma lakes are also called maria, and are composed of denser, iron-containing basalts. Many of the visible near-side maria are present in massive impact basins like Mare Imbrium, where the lunar crust was excavated by an impactor approximately the size of Wales (250 km diameter). These basaltic maria span the age of 3.8 G.A. to about 2 G.A., but meteorite fragments show the existence of lunar basalts as early as 4.35 G.A.[37]. This could mean that volcanic events were present earlier than previously assumed, but were destroyed by impacts.

Some areas of the Moon do not easily fit into the dichotomy of mare and terrae. Cryptomare are basaltic structures caused by volcanic activity that have since been covered by highland material [18], making them hidden from view. After the discovery of cryptomaria, the mare coverage of the nearside increased by 3% of the total lunar surface area, from 17% to over 20%. One way of dating a cryptomare is to identify the origin of the material covering it, as the impact that ejected material onto the then-uncovered mare must necessarily have occurred after the formation of the mare itself. Cryptomare allow us to investigate early Lunar volcanism and early evolution of the Moon in in general. They could potentially shed light on the question of what the mare creation rate was like in the time before the decline in impact rates, as the covered structures might be better insulated from further destruction by subsequent impact events due to it's thicker regolith[1].

1.1 Main scientific question

The radar measurements that are the focus of this study are the longest wavelength polarimetric inverse synthetic aperture radar measurements of the Moon to date. They were produced with the Jicamarca Radio Observatory (JRO) 6-meter wavelength radar in Peru [39]. The study identified two large regions, where the radar return was found to significantly deviate from the general pattern of mare and terrae. These two areas are the focus of this thesis work.

Figures 1.1 and 1.2 depict the JRO radar measurement, and an visual spectrum image of the Moon for the Northern and Southern hemisphere. The areas of interest, where long wavelength radar reflectivity significantly deviates from visual spectrum reflectivity is marked on the maps. Figure 1.3 shows the same maps using orthographic projection. The first anomalous region is located between Mare Frigoris and Mare Imbrium (F-I) in the Northern

1. **Regolith:** Upper layer of lunar surface

hemisphere. The other divergent region surrounds the ancient Schiller-Zucchius (S-Z) impact basin. Both of these regions have significantly lower depolarized radar return than other highland regions. As can be seen in the images, there is a general high correspondence between visual albedo and depolarized radar return.

The highlands generally have a high visual albedo while simultaneously being easy for radar wavelengths to penetrate due to their low content of chemicals that attenuate radio waves (TiO_2 and FeO). The opposite is true for the maria, with their high iron content and dark regolith. As a result, regions on the Moon that are bright in visual images tend to provide high depolarized radar return, while visually dark regions tend provide low radar return for long wavelengths. However, for some reason, the two regions identified in the 6-meter radar maps deviate from this general pattern.

The S-Z area has been studied before as it exhibited characteristics of being a cryptomare [3]. The cryptomare in the region was discovered to have an area approximately 6 % of the exposed mare surface, using the extent of dark halo craters in the area. Our earlier work showed a significant reduction in power in the ancient impact basin in this area, which supports the presence of a cryptomare. Due to the large halo of reduced depolarized return we hypothesized that the cryptomare might be much more extensive than previously found, as an extensive cryptomare is one way to explain the reduction in power.

The F-I highland has not been previously discussed in the context of cryptomaria. Neither has the region been discussed in the context of low depolarized return for long-wavelength radar either. As cryptomaria are one of the possible explanations of severely reduced depolarized power, we hypothesized that this area may be a very large cryptomare.

In this work, we will seek to explain the physical mechanisms that could cause the anomalously low radar return in the F-I and S-Z regions. We aim to study the possible physical mechanisms that could cause the reduction in depolarized power. If we are able to determine what causes the low depolarized return, this could give further insight into the historical development of the area being studied, and ultimately, the early evolution of the Moon and how radar remote sensing can be used to explore the lunar environment.

This study is interdisciplinary; combining lunar geology and long wavelength radar remote sensing. This study primarily focuses on ancient lunar volcanic manifestations, cryptomare, which can be obscured or covered by geological processes that have occurred at later times. Our primary methodology is application of long wavelength radar, which is known to be a powerful tool for probing the subsurface and discovering hidden features that are not otherwise

obvious. On the Earth, long wavelength radar measurements have been used to e.g., find subsurface aquifers buried beneath the Sahara desert [19] and to aid archaeological discovery. In our case, long wavelength radar observations will allow probing deep into the subsurface of the Moon, to study the subsurface composition of the Moon.

1.2 Relevance for the Norwegian school system

The benchmarks of competency are what defines the knowledge and skills students should acquire in the course of their education, which is defined by the Norwegian Department of Education [38]. One of these benchmarks for the high school science subject is: ”forklare hvordan elektromagnetisk stråling fra verdensrommet kan tolkes og gi informasjon om verdensrommet” (Utdanningsdirektoratet, 2013). This can be roughly translated as ”explain how electromagnetic radiation from space can be interpreted and how it can provide information about space”. This thesis relates to this in that it details interpretation and informational content of EM waves in the context of radar mapping. While the specific methods used here might be outside the scope of the class, general knowledge of radar methods and mapping can be part of achieving this competency.

The history and evolution of the solar system is something many students are interested in. Using this interest to motivate and encourage students to both learn science and enjoy the learning process can help recruitment to higher levels of science education.

My father once told me a story about his high school music teacher that made an impact on him. All the previous lessons in music would be a tired teacher playing vinyls and lecturing the class about the origins and meaning behind it. His new teacher once asked the class who had heard of the Ballad of Revolt (Kjempeviseslåtten). When none of the students had, the teacher played it himself on the piano. My father said that knowing his teacher could actually create music, not just talk about it while it played on vinyl made a great and lasting impression on him. Therefore, while the subject matter in this thesis might not relate very well to the specifics of competency directed by the Department of Education, the knowledge and methods gained while working to create it may help me inspire students in the same way.

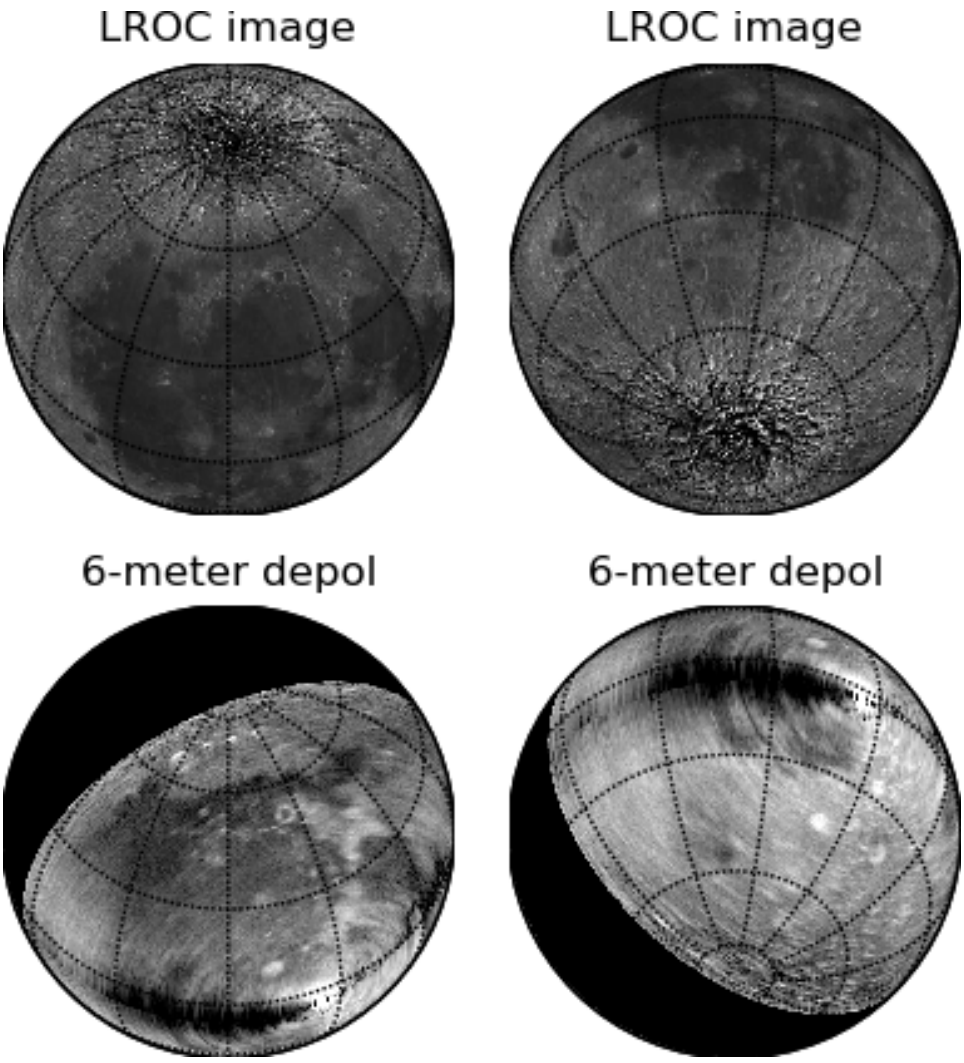

Figure 1.3: A comparison of optical images from the LROC and depolarized radar SAR images by Vierinen et al. Top left: image centered on the highland region between Mare Imbrium and Mare frigoris. Top right: image centered on the Schiller-Zucchius basin on the southern hemisphere. Bottom left: depolarized SAR image centered on the highlands between Mare Imbrium and Mare frigoris. Bottom right: depolarized SAR image centered on the Schiller-Zucchius basin.

1.3 Overview of this work

In order to answer the reason for the mysterious radar dark regions on the Moon, we have formulated several hypotheses that could explain the measurements. In order to test these hypotheses, we have compared the 6-meter wavelength radar maps with other auxiliary measurements of the Moon, which provide information about the geological properties of the Lunar surface. We have used visual images gathered by the Lunar Reconnaissance Orbiter Camera (LROC), radar data gathered by the SELENE (also known as Kaguya) Lunar Radio Sounder instrument, a 70-cm wavelength radar map with the Arecibo radio telescope, and multi-spectral measurements of surface geochemical composition. We have also developed a radar scattering model to analyze how radio propagation losses and resonant scatterers within a volume affects the the measured radar cross section.

The structure of this thesis is as follows:

- Chapter 2: Background. This chapter provides the necessary background information and organizes the previous research that will be used to answer our question.

- Chapter 3: Method. This chapter describes the way in which we investigated our main scientific problem. Here we present three hypothetical solutions and describe how we will test them.

- Chapter 4: Results and discussion. In this chapter, we present our findings for each hypothesis and discuss what this implies for our main scientific question.

- Chapter 5: Conclusions. We discuss our findings and relate them to previous research. We also discuss what remains unanswered, and what future work could done to reach closure on the remaining open questions.

2 Background

This chapter will present the background knowledge needed to understand our main scientific question, and the methods we use to explore it. It contains information about lunar geology and how the surface properties of the Moon has changed through time. There is also a section on previous radar studies on the Moon that are relevant to this work, as well as visual and multispectral analysis. We will also describe the specifics of the Jicamarca experiment and range-Doppler mapping.

2.1 Lunar Geology

The chemical composition of the Moon is almost identical to that of the Earth, a fact supporting the “big splash” hypothesis of the origin of the Moon, where Earth collided with a planetesimal called Theia, and a mixture of both objects created both the Earth’s crust and the lunar crust. Since then, the lunar surface has been shaped predominantly by impact events and early lunar volcanism on the nearside, creating two distinct terrain types. These are the basaltic maria, which are remnants of lava lakes, and the regolith highlands formed by the destruction of a slowly cooling lithosphere suspended over a magma ocean in the early history of the Moon.

2.1.1 Surface Evolution

Figure 2.1 illustrates how the lunar surface is thought to have evolved over time. In the early history, the lunar surface was not stable enough to form a lithosphere[1] due to high temperatures and frequent impact events. Any structure, either formed by impact events such as craters, basins, and impact melts, or volcanic structures like basaltic flows, were destroyed by subsequent impacts. Later, when impact events became less frequent and the Moon cooled down, a lithosphere of broken rock formed, called the megaregolith. As the cratering rate had declined, structures like volcanic flow complexes and large impact basins were no longer being broken down and gardened. Due to this, they survived, and are still visible today as the large dark regions on the near side of the Moon.

2.1.2 Mare and Terrae

The terra and mare surface types of the Moon are generally very distinct from each other, and tend to be similar to themselves. Terrae are composed of anorthosites and tend to be heavily cratered. They are generally also at higher elevations than the maria. The maria are composed of basalts and tend to be less cratered than the highlands. There is a much larger extent of maria on the nearside than the farside. They tend to be in low-lying areas like impact basins.

Anorthosite is a rock type composed mainly of feldspar (K, Na, Ca)$AlSi_3O_8$. This mineral composes the primary part of most rocky planet crusts, and is composed of some of the most abundant elements in the Earth's crust[14]. This is particularly true for the Moon, where anorthosites account for nearly all the visible crust aside from the basaltic mare. This has been determined by physical samples brought back from the Apollo missions as well as multispectral imagery used to detect the surface composition [11]. Anorthosites are characterized by being very light with a density between 2600 and 2800 g/L (in comparison, liquid iron has a density of 7874 g/L). During the early differentiation of a planet, these minerals will readily float to the top of a magma ocean, which is one of the proposed reasons why they are so common in planetary lithospheres.

Basalts are a class of rocks which form when iron-rich magma originating from within the depths of the Moon cools rapidly. They are fine-grained and dark, and in the case of the Moon, generally have an iron content between 15% and 23%. Lunar basalts are also classified by their titanium content into high-

1. **litosphere:** solid crust of unmolten, nonviscous material

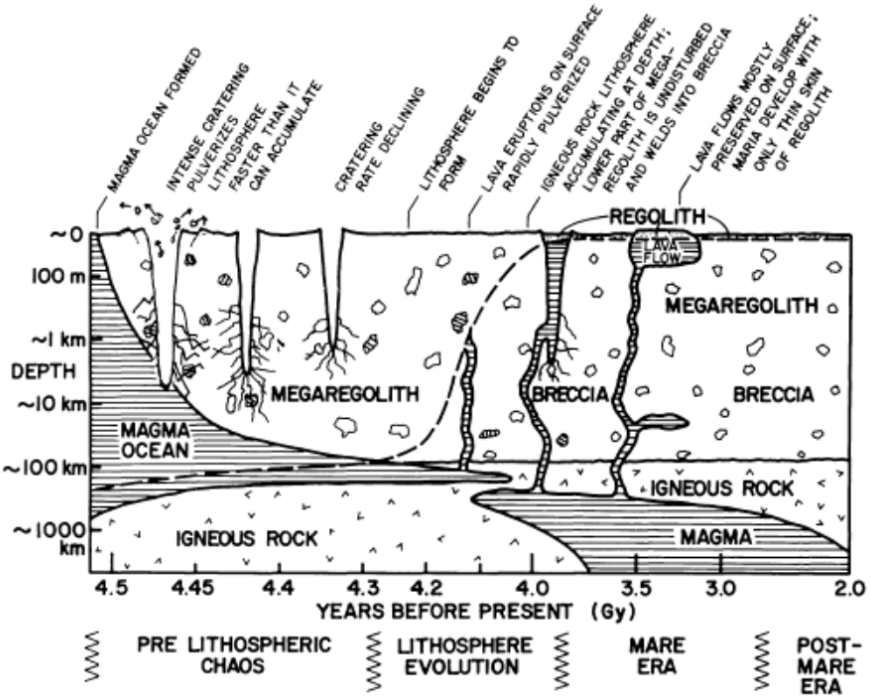

Figure 2.1: Visualization of lunar surface and megaregolith evolution over time by Hartmann [17]. The dashed line represents the regolith production rate over 100 My. The early crust was broken apart by impact events, leaving a thick layer of broken or agglutinated rock. Volcanic structures were likewise destroyed, until the cratering rate declined enough for structures to survive to the current day. Note that x-axis does not have a constant scale. Figure used with permission from author.

titanium, low-titanium and very-low-titanium basalts, where the low titanium variant is the most common on the Moon. These types of rock generally form by volcanic eruptions expelling magma onto the surface, where it spreads and cools relatively rapidly.

2.1.3 Structure of the Lunar surface

The lunar crust consists of several different layers, according to Heiken et al. [20], see figure 2.2. Long wavelength radar will be more influenced by the large scale ejecta layer since the majority of the volume probed by the wave will be in this layer. While the exact size distribution of rocks in the lunar crust is unknown, we assume that it does not change radically from one area to the next. While highlands and maria can have significant differences in structure, it is assumed that all highlands are relatively similar, and all maria are relatively similar. This leads to the conclusion that the depolarized return in highland regions primarily originates from rocks of varying size suspended in the lunar crust. In order to further characterize the rocks that are of interest to us, we created a simple model for the radar cross section of a volume filled with rocks of different diameters, which will be presented in chapter 3.

2.1.4 Cryptomare

Cryptomaria are special cases for the lunar surface [18]. These are areas where a basaltic mare has formed, but has been covered by highland materials at a later time. According to Whitten and Head [41] there are four different types of cryptomare, see figure 2.3.

First are Copernicus-type cryptomare, which are created when an impactor is large enough to pierce entirely through the basaltic slab, and excavate highland material buried beneath the mare. This highland material is ejected and covers the mare some distance around the crater.

Second are Balmer-type cryptomare. These are caused by several impact events in highlands surrounding a mare. These impact events eject highland material onto the mare, obscuring it from view.

The third and fourth type of cryptomare are proximal ejecta cryptomare and distal ejecta cryptomare, which are both cases where an impact event in a highland region scatters anorthositic material onto a basalt plain, concealing it. The difference between these two classifications whether the impact event occurred near the mare or far away from the mare. Note that this classification is somewhat subjective and leaves room for interpretation.

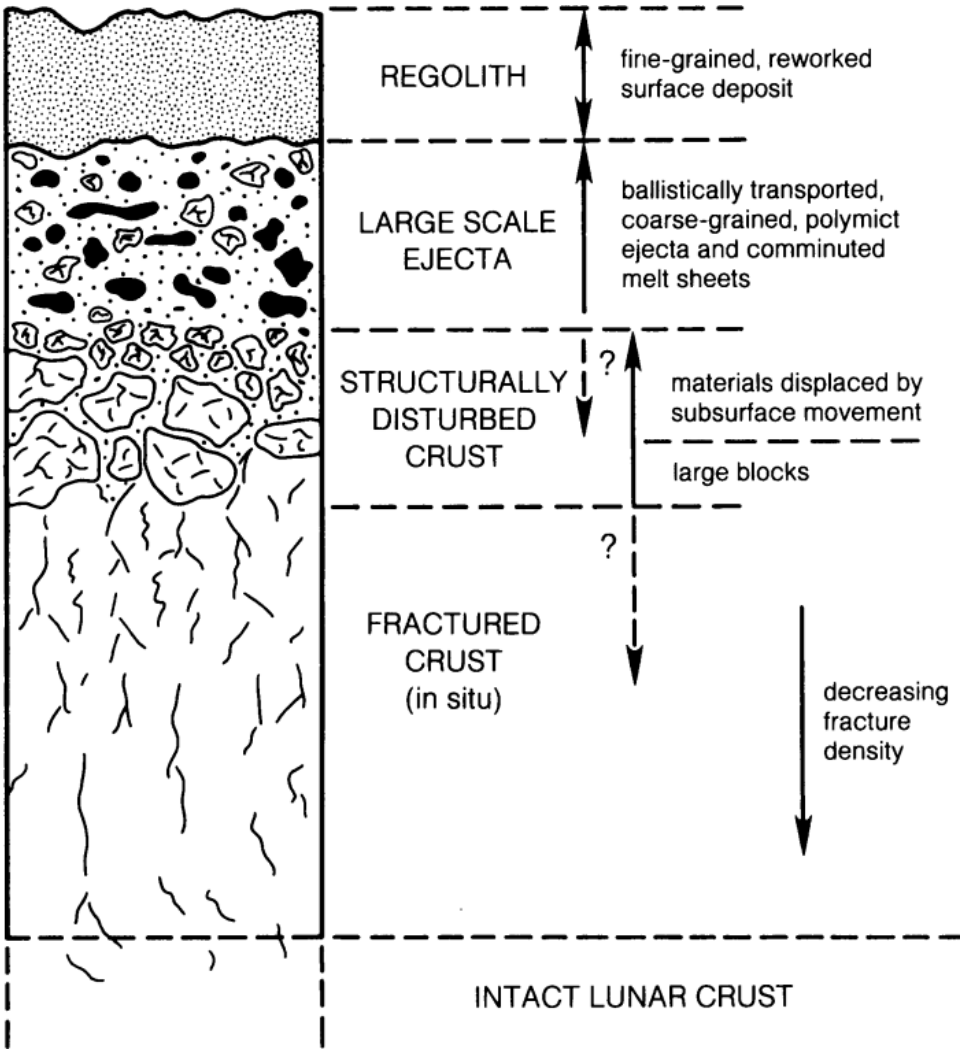

Figure 2.2: Layers in the lunar crust. The first layer is very fine dust which might be 10m deep, followed by a layer of larger rocks from impact ejecta and broken crust to a depth of about 2km. Below there is a layer of large rocky blocks and displaced crust caused by subsurface movements, as deep as 10km. The depth scale of these layers is highly uncertain and vary between estimates, and no hard boundary has been detected, rather a gradual change with depth [20].

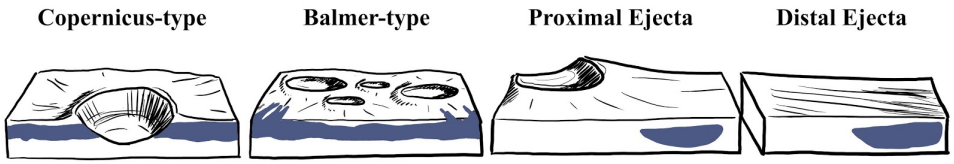

Figure 2.3: This figure shows the four different classes of cryptomare. From Serrano, personal communication, 2019.

After a cryptomare has formed, subsequent impact events that strike the covering regolith could excavate and reveal mare materials, which could assist in discovering it. If subsurface materials aren't brought to the surface, the area will be erroneously classified as normal highlands. Observation methods that penetrate deeper into the medium can detect the buried layer. Of these two deviating regions identified in the JRO study, The S-Z region has been identified as a potential cryptomare. However, the much larger and more striking Frigoris-Imbrium region had not previously been identified. This measurement is the first observation of polarimetric low frequency radar return of the Moon, providing valuable new information about the subsurface composition of the Moon.

Lunar mare formation appears to have started very suddenly around 3.8 GY. Primordial mare deposits from a time before this would show that the history of lunar volcanism started before this. If a mare deposit is covered by ejecta from an impact event, the mare deposit must necessarily have appeared before the impact event. Cryptomare are then useful for dating the volcanic history of the lunar landscape [41]. Cryptomare have previously been detected through dark halo craters and chemical analysis of the regolith layer. Impact events in cryptomare areas can penetrate the anorthositic cover and excavate mare basalts, which can be seen in visual images and short-wave radar images. Chemical composition can also be used to show the presence of basaltic materials in the anorthositic layer. Mixing in the regolith cover of a cryptomare can drive basaltic components to the surface, where it can be detected by multispectral imaging. This method can also point to possible cryptomare regions if the regolith has unusually large basaltic components not attributed to dark halo craters or ejecta from mare impact events.

Lunar soil texture is modified by three processes. Impactors excavate several times their own mass of lunar material, spreading it over the surrounding area. This will mix the upper layers of the lunar surface, as well as breaking apart

large structures such as boulders and mountains. Micrometeoroid impacts will chip away at rocks and objects on the surface, but due to their small mass won't mix the regolith to a significant degree. Any impact event can also heat the surface material, melting particles and forming agglutinate particles or glass. Solar wind can also cause erosion of exposed surfaces. For this work, the important aspects here are that large impact events bring large-scale detritus from the deeper layers of the crust to the surface, and mix the composition of upper soil layers with the deeper crust, while micrometeoroid impacts and space weathering will wear down structure over time, forming a fine dust.

2.2 Lunar remote sensing

In this section, we discuss remote sensing techniques for observing the Moon. We will discuss methods and techniques used for the Jicamarca observation in more detail in a later section.

2.2.1 Visual Spectrum Imaging

As the Moon is tidally locked with Earth, only the nearside is visible from Earth's surface. With the invention of the telescope, the first attempts at mapping the craters and ridges of the lunar surface began [10]. A lot of progress has been done since then, notably by the soviet spacecraft Luna 3 [2] which was the first to bring images of the lunar farside back to Earth. It was discovered that the farside is significantly different than the nearside with the near-total absence of mare formations.

Lunar satellite missions were also able to make more detailed images of the Moon, which resulted in the more accurate surface maps both of visual albedo and topography [26]. The NASA Lunar Orbiter 4 aided in the discovery of the impact basin Schiller-Zucchius [16].

For this study, we have used images from the Lunar Reconnaissance Orbiter Camera provided by the LROC Science Operations Centre team at the Arizona State University, courtesy of Robinson et al. [32], Humm et al. [21], Mahanti et al. [25], and Speyer et al. [35].

2.2.2 Multi-spectral imaging

Lunar surface chemical composition has been studied using wavelengths ranging from the near infrared to ultraviolet [11]. Of interest in this thesis are

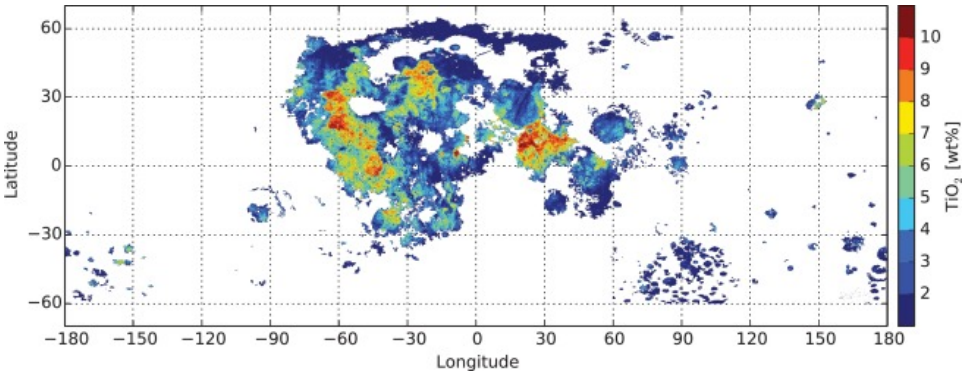

Figure 2.4: Global map of titanium (TiO_2) concentration of the lunar surface by Sato et al. [34]. Any concentration below 2% is undetectable by this method.

global maps of TiO_2 and FeO content. These estimates are made by creating multispectral reflectance images of the lunar surface, and comparing the resulting reflection spectrum to the measured reflection functions of iron oxide and titanium dioxide.

Sato et al. [34] has created a global estimate of the lunar surface titanium content (see figure 2.4). It is worthy of note that highlands generally and the radar-dark areas being investigated specifically have low enough titanium content to be below detection limit. Mare Frigoris has very low titanium content, where the majority is between 0 and 2 %. Both Mare Imbrium and Sinus Iridum are on the low end of the scale, with the exception of the bright red spot on the western edge of Mare Imbrium.

Iron content studies have been done by Lucey et al. [24]. As with titanium dioxide, iron oxide is much more prevalent in the maria than the highland regions, though there are detectable quantities also in the highlands, see figure 2.5. The Highland region near the Schickard crater has elevated iron content with areas above 10 % by weight. In the north, the F-I region shows values well above normal highlands, but not uniquely so. Mare Imbrium shows values reaching 20 %, while Mare Frigoris is generally between 10 and 15 %. In general, highlands show values that are between 0 and 5 %.

It is worthy of note that visual and multi-spectral studies are limited to only the top layer, as light in the infrared and visual spectrum does not penetrate an appreciable distance into the lunar regolith. This means that these studies can only give an answer to what the chemical composition is like in revealed regolith, which might be different from the chemical composition found in the deeper layers of the lunar crust. It is therefore difficult to be certain that calculated penetration depths are valid for longer wavelength radar studies, as

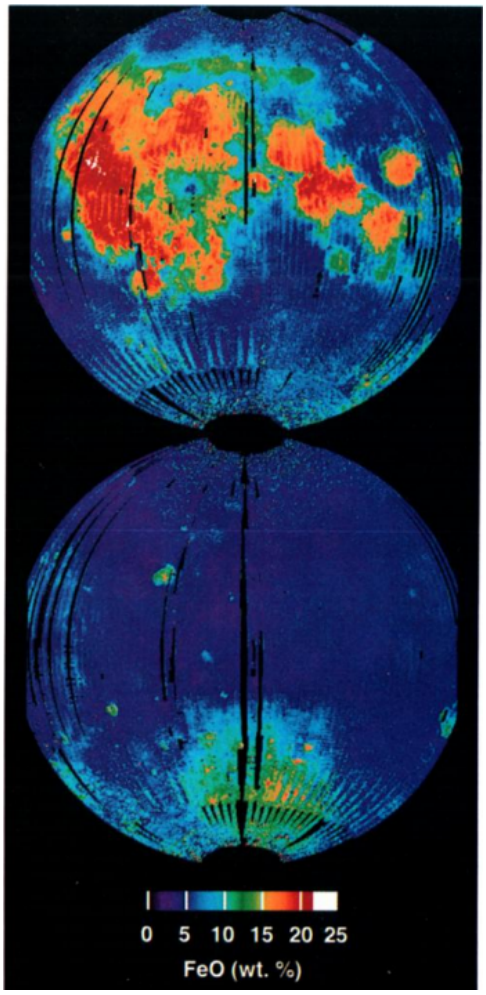

Figure 2.5: Iron oxide content by weight across the lunar surface. Top of figure shows the lunar nearside and bottom shows the farside. Note that the F-I region has an iron composition between 5 and 10 % by weight, similar to the highland region between Mare Imbrium and Lacus Somniorum, east of Montes Alpes. To the south, there is an area surrounding the Schiller-Zucchius basin with iron content around 10 %.

the loss tangent of the medium could vary significantly as the signal penetrates deeper into the crust.

2.2.3 Planetary radar studies of the Moon

Due to the challenges of making in-situ measurements of non-terrestrial surfaces, remote sensing is a useful tool for data collection. Radar measurements can provide information about the albedo and scattering properties of the surface being studied. This can then be used to infer other properties of the surface, like roughness, structure, chemical composition and subsurface structure.

As radar allows a wide span of wavelengths, it is possible to explore these properties at different scales. The roughness of a surface seen with 60 m wavelength can be substantially different from the roughness of the surface as seen with 12 cm wavelength.

A radar map of a planetary surface will contain information about the radar cross section of the surface as seen from the radar. This will depend on both the material and the structure of the surface [4]. Further information is contained in the polarimetric information that can be obtained by recording orthogonal polarizations. This information can help differentiate which scattering mechanism is responsible for the scattered power, based on which scattering mechanism causes the different observed polarizations.

For our purposes, the polarization state of can either be polarized or depolarized, which represent the polarizations that maximize and minimize the sub-radar point echo, respectively. This was done because we assumed the sub-radar point is mirror-like, in which case the specular scattering mechanism would dominate. Due to the smoothness of the lunar surface, we have assumed that polarized returns are mostly comprised of surface scattering, and the depolarized returns are mostly caused by volume scattering.

There have been multiple previous radar studies of the Moon on a variety of wavelengths, starting shortly after the invention of radar [28]. The evolution of planetary radar helped improve our current knowledge of the lunar surface by investigating areas like the permanently shadowed craters near the poles to look for water ice [36].

Earth-based radars have been used for a wide range of topics in the field of planetary science. In 1964 a continuous-wave radar was used to determine the rotation of Venus [7]s, and found the surprising result of retrograde rotation with a period of 230 days. Radar measurements were also used to determine

the progression of Mercury's perihelion in an experiment that confirmed the predictions of general relativity [29].

Other useful results from planetary radar studies of the Moon are the detection of buried layers in the nearside maria by Oshigami et al. [31], and Earth-based radars have been used to measure the roughness of the lunar surface [13]

The radar maps most relevant to this thesis were done by Vierinen et al. [39] and Campbell et al. [5]. These are polarimetric readings of the lunar surface at 6 m wavelength and 70 cm wavelength, respectively.

Dielectric loss and the lunar soil

The dielectric loss of a material as a function of composition is of special interest to us, when studying volume reflectivity of a radar map.

The lunar landscape has a clear dichotomy in the visual spectrum, with bright, anorthositic highlands and dark, basaltic maria. This difference is also visible in the depolarized radar return on 6 meter wavelengths, where highlands are composed of fragmented, low-loss anorthositic materials which provides ample opportunity for the wave to scatter back to the antenna, while the maria are smoother, lossy terrains providing very little depolarized radar return.

The loss tangent [4] of lunar material was experimentally determined based on samples gathered by the Apollo mission to be [20]:

$$\tan\delta = 10^{(0.045[\%\mathrm{TiO_2}+\%\mathrm{FeO}]-2.754)}. \tag{2.1}$$

In this equation, %FeO denotes for the iron oxide concentration by weight and $\%\mathrm{TiO_2}$ the titanium dioxide content by weight. This relation was found for 450 MHz, and a plot of measured loss tangents showed that there was a minimum for the loss tangent function near 10 MHz. However, we were unable to find an expression of the loss tangent corresponding to 6-meter wavelength. According to Heiken et al. [20] the loss tangent for 5 MHz and 50 MHz waves will be lower than what is found by the formula they present. If we assume a loss tangent equal to what is found when using this formula, we can be sure that we do not overestimate our penetration depth.

Penetration depth

The penetration depth of an EM wave can be defined as the depth at which the field intensity of the wave is reduced to $I(r) = 1/e \cdot I(0)$. Since power is the square of the electrical field, the power is then reduced to $1/e^2$. An

electromagnetic wave's intensity varies by distance as $I(z) = I(0) \cdot e^{-\alpha \cdot z}$, where alpha is the attenuation factor. a distance $\rho = 1/\alpha$ is the depth at which the amplitude of the signal has attenuated to $1/e$. α is found by $\alpha = 4\pi/\lambda \cdot im(n(\omega))$, where $im(n(\omega))$ is the imaginary part of the refractive index for the frequency of the signal. One issue with this calculation is that the refractive properties of the Moon vary based on chemical composition, and the penetration depth can vary from tens of meters to several kilometers with a 6m wavelength wave.

Frequency (λ)	HTB e-fold	LTB e-fold	Highland e-fold
5 MHz (60 m)	160 m	380 m	4100 m
50 MHz (6 m)	16 m	38 m	410 m
430 MHz (70 cm)	1.9 m	4.4 m	48 m

In table 2.2.3 we have calculated penetration depths for three different lunar surface types at the three wavelengths that are of primary interest to our work. In high-titanium basalts (HTB) the e-folding distance is generally extremely low due to the high concentrations of both iron and titanium. Low-titanium basalts (LTB) have longer penetration depths due to their comparatively lower titanium content, while highlands have the longest penetration depths. It is important to remember that the exact values will be unknown due to the generally poor knowledge of how the chemical distribution varies by depth, as well as the probable case where the model used to calculate the loss tangents do not directly apply to the frequencies in question. In that regard, the 430 MHz estimate is the best, as it is close to the frequency used to create the empirical model of loss tangent as a function of chemical composition.

Scattering law

The Hagfors scattering law describes the power spectrum of a smooth target which is much larger than the radar wavelength as a function of the angle of incidence [9]. The relation is stated as:

$$\sigma(\phi) \propto \left\{ \frac{1}{\cos^4 \phi + C \sin^2 \phi} \right\}^{3/2} \tag{2.2}$$

where $C = (d'\lambda/4\pi h_\circ^2)^2$. In this expression, σ is the power spectrum, ϕ is the angle of incidence, and C is a measure of the scale of surface variations in proportion to the wavelength.

Figure 2.6 shows a collection of scattering law measurements of the lunar surface at varying wavelengths. The shape of the curve is determined by the roughness of the surface in proportion to the wavelength. When the wavelength increases, the returned power decreases faster as a function of

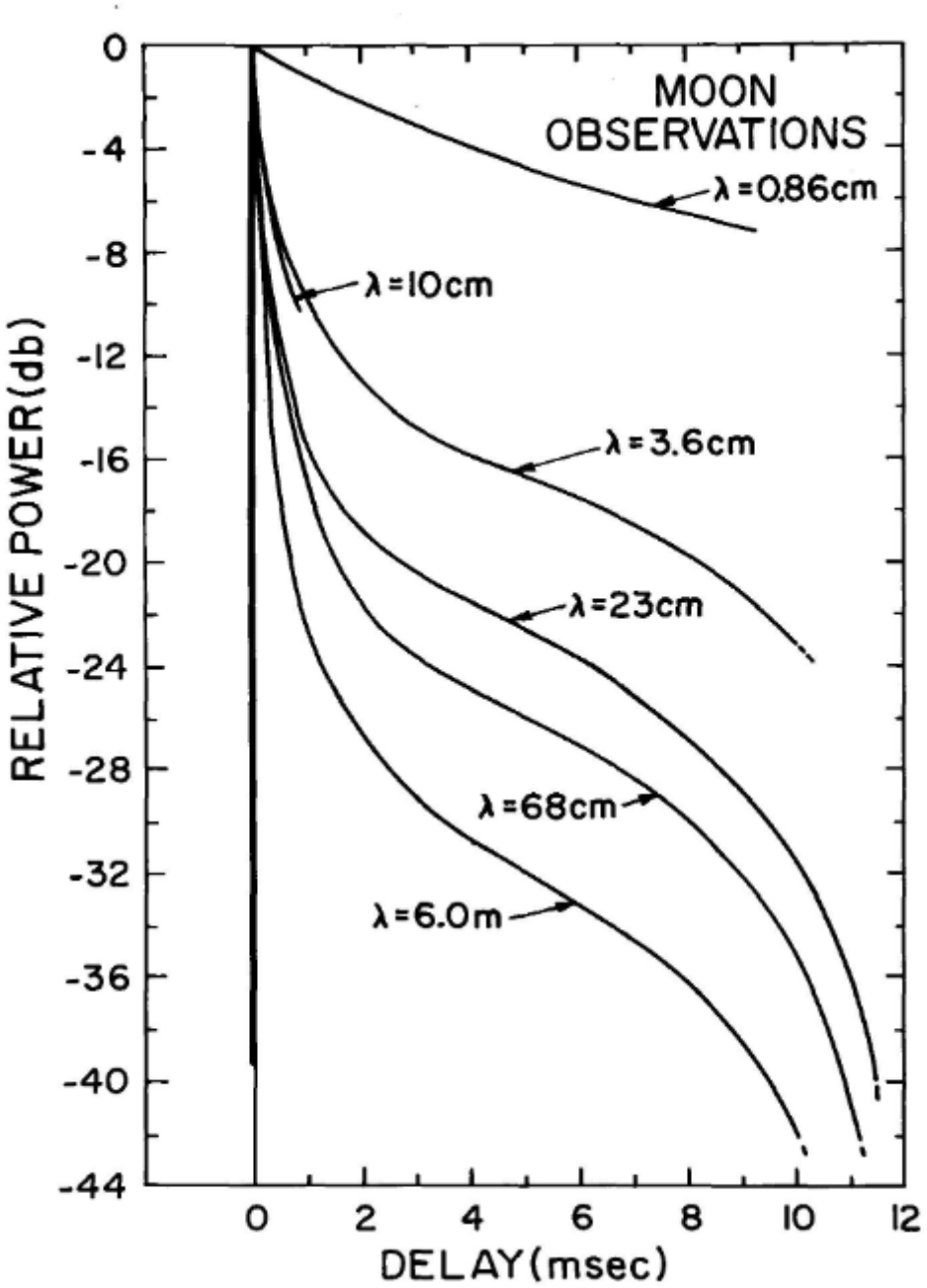

Figure 2.6: A plot showing experimental estimates of the Hagfors scattering law for the lunar surface, using delay as analog for angle of incidence, provided by Evans and Hagfors [9].

the angle of incidence. This is caused by the roughness of the surface, where the longer wavelengths only probe large surface structures. The power in the returned signal is primarily carried in the specular polarization, so structures that effectively reduce the angle of incidence to zero in regions where the surface tilts away from the receiver due to the curvature of the Moon will significantly increase the returned power. An important quality of the scattering law is that if expressed as the power spectrum as a function of the target depth of a spherical target, each range gate will have the same area. If projected by scattering angle or latitude, however, one must correct the area in this projection.

2.2.4 Radio sounding

The Apollo missions already carried HF radio sounding instrument (ALE) to study the subsurface of the Moon. Similar instruments have also been used to study the subsurface of Mars (MARSIS, [22]). The most recent mission to include an HF radio sounding instrument to study the surbsurface structure of the Moon was onboard the Kaguya mission (LRS, [30]).

This radar used a 60 m wavelength single-polarization and scans in frequency for pulse compression. The data used was processed to obtain the nadir echoes showing slices of the lunar crust along the satellite's path, which enables us to see the apparent depth of reflections detected by the satellite. In figure 2.7 there is an example plot of LRS data, and drawn lines to show detected subsurface reflections believed to be from continuous substrates.

In this study, we have used data from the Kaguya LRS instrument. As the radio wave is not traversing the ionosphere, the interference issues experienced in the JRO experiment is avoided. This allows it to use a 5 MHz wave, penetrating even further into the lunar subsurface.

The LRS instrument is particularely suited to detecting subsurface structures like basaltic layers or magma tubes, as these formations will have such a high loss tangent that Earth-based radars will have trouble penetrating far enough into the covering regolith to detect them, and will also have issues achieving a resolution sufficient to resolve these structures.

One of the central themes of this thesis is the study of cryptomaria, as it was presented as a possible explanation in our previous work. Therefore, the subsurface probing ability of the LRS can prove a valuable tool for our investigation in the S-Z and F-I regions. Potential subsurface structures detected by the JRO study should also be visible to the 5 MHz wave. The addition of a lower frequency to the span being investigated can also provide useful

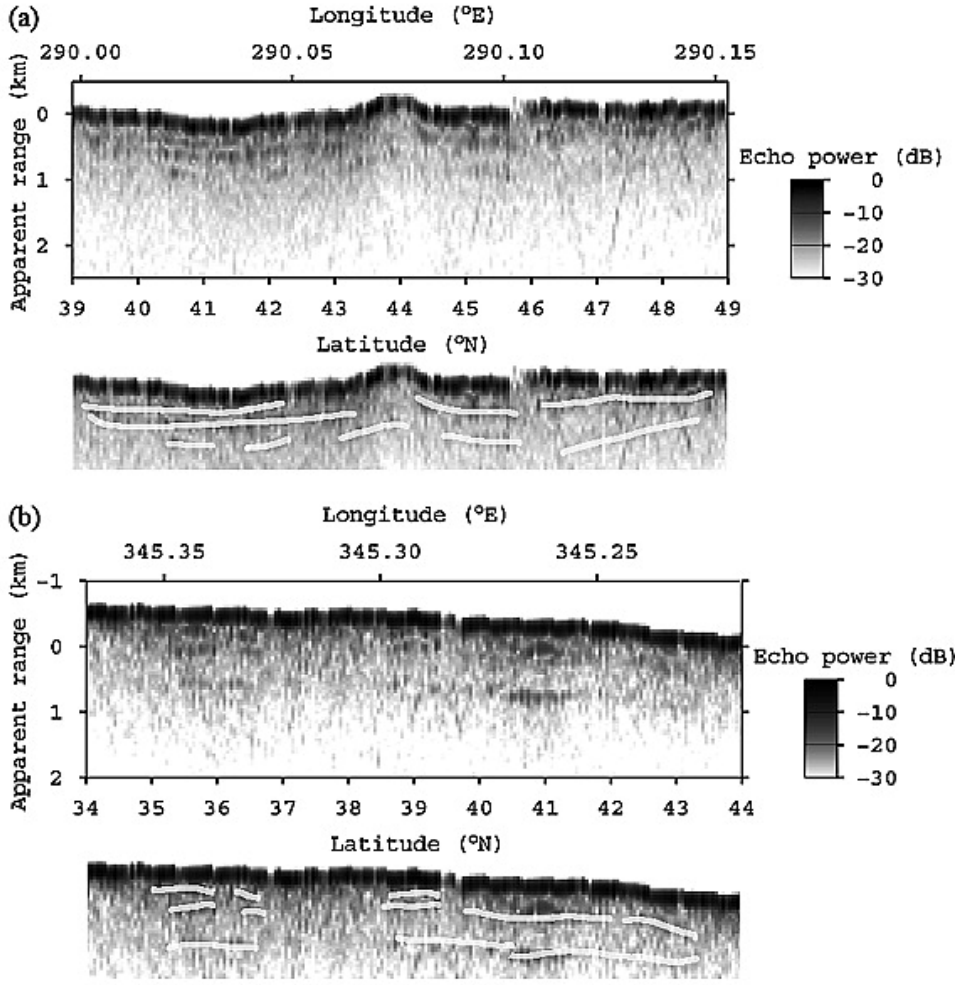

Figure 2.7: This figure shows data from the LRS instrument used to show the presence of subsurfaces in a) Mare Imbrium and b) Oceanus Procellarum. Figure taken from [31].

information about the depth at which the effect is present.

2.3 Jicamarca Inverse Synthetic Aperture Radar Mapping

Jicamarca is a phased array radio telescope located outside Lima, Peru, coordinates 11.95°S, 76.87°W with an elevation of 520 meters above sea level. It is run by the Geophysical Institute of Peru, primarily for ionospheric measurements. The radar has previously been used for lunar scattering law measurements[12][23]. It consists of 18432 dipoles in a square arrangement of side-length 291 m.

The antenna is a phased array, which can be steered ± 3° from it's on-axis alignment. However, the steering is analog and cannot be done on short enough timescales to actively track the Moon. During the experiment, only the eastern quarter was used to transmit at a peak power of 600 kW in order to increase the beamwidth to 2° to increase the illumination time due to the lack of steering. The map was created using the data gathered from the modules furthest north and furthest south in order to achieve a 360.7 m interferometric baseline to resolve the range-Doppler ambiguity. The East and West quarters were also recording data, but have not been used for mapping purposes.

The radar transmits on a frequency of 49.92 MHz, which corresponds to a wavelength of 6.01 m. The transmitter is capable of transmitting in any polarization. In our experiment, the transmitted polarization was circular while the radar received in orthogonal linear polarizations. A 169-bit transmit pulse was used, which was formed using the Kronecker self-product of a 13-bit Barker code, giving each pulse a total duration of 1.69 ms and a 10 μs baud length [39]. This means that one can deconvolve the transmit pulse and transform the 1.69 ms signal into a 10 μs signal, compressing the energy of the signal. This is done to increase signal-to-noise ratio of the Lunar echoes. The interpulse period was 39 ms in order to keep the Moon from aliasing into the ionosphere or the transmit pulse during the experiment.

The Doppler spread caused by the apparent lunar rotation is approximately 1.4 Hz. This means that the Moon can be assumed to have zero Doppler migration or spread during a single 39 ms period. The total Doppler migration over the entire observation period is also sufficiently small to be negligible.

2.3.1 Pulse compression and deconvolution

When a radar pulse is scattered by a surface, properties of the signal are changed. This mechanism is described by a convolution process, where the signal $T[t]$ passes through the surface system $S[t]$. The output signal is then $R[t] = T[t] * S[t]$ (see figure 2.10). T[t] is the transmitted pulse, $S[t]$ is the scattering function of the target body and $R[t]$ is the returned signal. The symbol $*$ denotes convolution in the time domain. In order to remove the transmit function from the returned signal, an inverse filter is used. Inverse filtering is a process where deconvolution is done in the frequency domain as pointwise division. This is done by Fourier transforming the obtained signal as well as the transmit pulse, in order to manipulate the function in the frequency domain. Fourier transforms are a process which expresses a time series as a function of the various frequencies that together produce the sampled series. The convolution theorem states that convolution in time domain is the same as point-wise multiplication in frequency domain, and it follows that division in frequency domain is deconvolution in time domain. Therefore the system function is found as the division of the returned signal with the transmitted signal:

$$\frac{R(\omega)}{T(\omega)} = S(\omega). \tag{2.3}$$

This function will then give information about the surface properties of the Moon.

2.3.2 Range-Doppler mapping

When illuminating an object with a radio pulse, the distance to the object illuminated is found through light travel time. Since the Moon is approximately spherical, there will be a continuous ring of points centered on the sub-radar point that are the same distance away from the observer. It is impossible to use range information to distinguish any point on this ring from any other. The motion of the object, relative to the observer, is found by a Doppler-shift in the reflected wave. Since the Moon is rotating relative to the observer, one limb will be approaching the radar array, while the other will be receding, once the bulk range-migration is removed. This causes half of the lunar surface to have a negative Doppler-shift, while the other half will be Doppler-shifted positively. The Doppler shift is proportional to the motion towards the observer, and the motion towards the observer is found by equation:

$$R_m \cdot \cos(\text{lon}) \cdot \sin(\text{lat}) \cdot \omega \tag{2.4}$$

In this equation R_m is the lunar radius, approximately 1738 km, lon is the apparent rotational longitude (zero for sub-radar point) and lat is the apparent

rotational latitude (zero for sub-radar point), while ω is the apparent rotation rate.

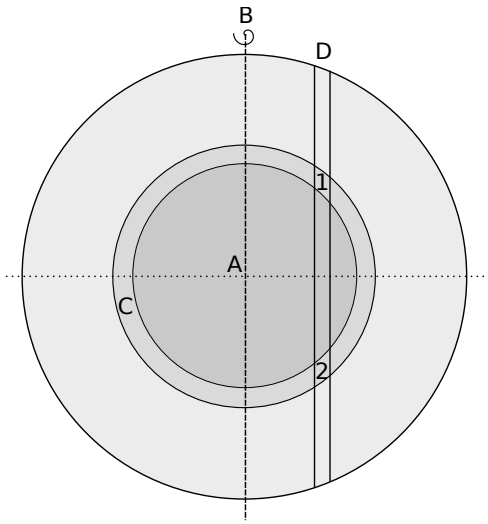

Figure 2.8: In the figure above, the range-Doppler ambiguity is demonstrated. A spherical target is shown, rotating around the axis denoted B. A range cell is shown as C, and a Doppler cell is shown as D. All points on a circle centered on A will have equal range to the radar, and all points on a line parallel to the rotation axis B will have equal Doppler shift. This means that for any point on the upper half of the sphere, there will be a point on the lower half with identical range and Doppler information, like points 1 and 2 denoted in the figure.

2.3.3 Range-Doppler ambiguity

In figure 2.8, we see a spherical rotating target head-on. The sub-radar point is denoted A, in the middle of the figure. B is the rotation axis. C is a band located between two concentric circles of equal range, which is used to illustrate a band of range-resolution. D is a band located between two lines of equal instantaneous velocity away from the observer, which is used to illustrate a band of frequency resolution. The points 1 and 2 each lie in the band D and the band C, and therefore contain the same range and Doppler shift information, and are therefore indistinguishable when looking solely at these variables. Every resolution cell on the northern hemisphere will have a corresponding resolution cell on the southern hemisphere with identical range-Doppler information, causing the map to ”fold” along the apparent equator unless the range-Doppler ambiguity is resolved.

In order to resolve this ambiguity we use the Rogers and Ingall’s technique

[33]. This is a method for resolving the range-Doppler ambiguity. This method makes use of two antennae separated by a distance in the apparent north-south direction of the target body. The distance from each antennae to points on the target body will be slightly different, which will introduce a phase shift in the measured field. This phase shift is smaller the closer the points are to the Doppler equator, making it near impossible to resolve the area immediately surrounding the Doppler equator.

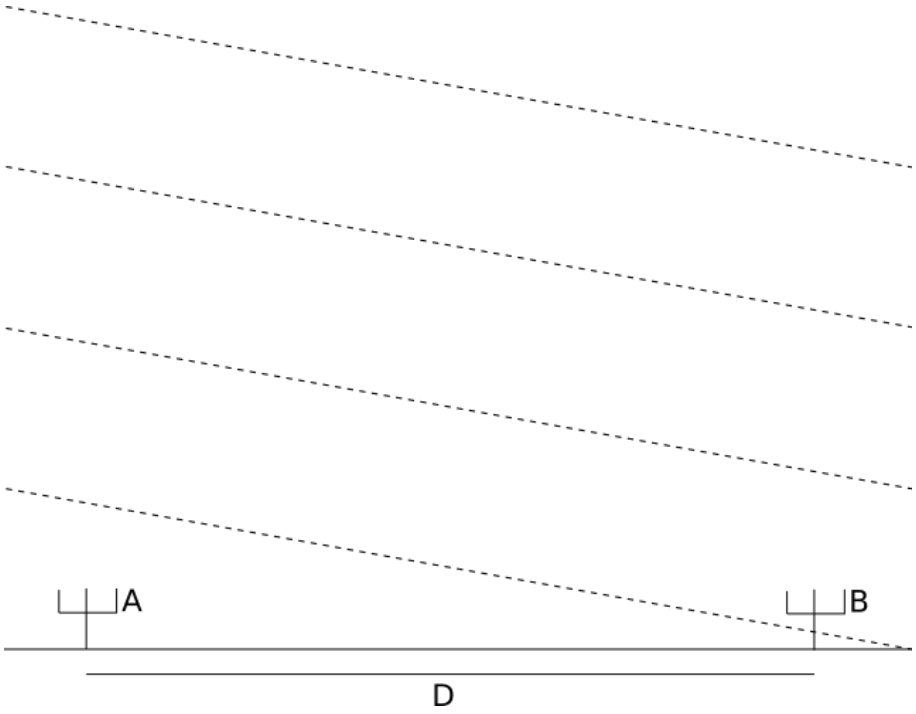

Figure 2.9: Visualization of interferometric range-Doppler deambiguation. The dashed lines are wavefronts of equal phase. The phase difference between antenna A and antenna B is caused by the distance along the apparent rotation axis denoted by D in the image. The phase difference will be different for the north and south hemisphere, allowing one to differentiate ambiguous points as in figure 2.8.
In 2.9 we see a visualization of the phase difference introduced by having two antennae separated by a distance D in the apparent north-south direction.

2.3.4 Radio propagation

Since Jicamarca is near the equator, the radio wave is directed nearly normal to the geomagnetic field. This means that the signals are Faraday rotated to nearly linear polarizations.

Another issue is the refractive properties of the ionosphere. When a radio pulse passes through the ionosphere, it is refracted slightly, changing the frequency by fractions of a hertz. This means that the returned signal has a Gaussian distortion in the frequency domain, giving point-like targets, which should only have one single Doppler shift, a Gaussian distribution of frequencies. In order to combat the effects of this disturbance, we have used the a-priori knowledge that the sub-radar point has no Doppler shift once the bulk motion of the Moon has been removed. We convolved each pulse with a sinusoid with the frequency spectrum found of the sub-radar point, thereby focusing the entire lunar surface with this frequency spectrum. This will not be completely accurate for the entire lunar surface due to spatial variations in the plasma frequency, but it will remove a large portion of the ionospheric noise.

2.3.5 Range aliasing

Range aliasing occurs when sending multiple pulses with an inter-pulse period (IPP) shorter than the pulse transmit time. After sending some number of pulses, echoes will reach the receivers, but the observed range will "fold" such that it is between 0 and ipp $\cdot\, c/2$. In other words, the observed range is found as $\mathrm{mod}(Ra, \mathrm{ipp} \cdot c/2)$, where Ra is the true range and c is the speed of light. In

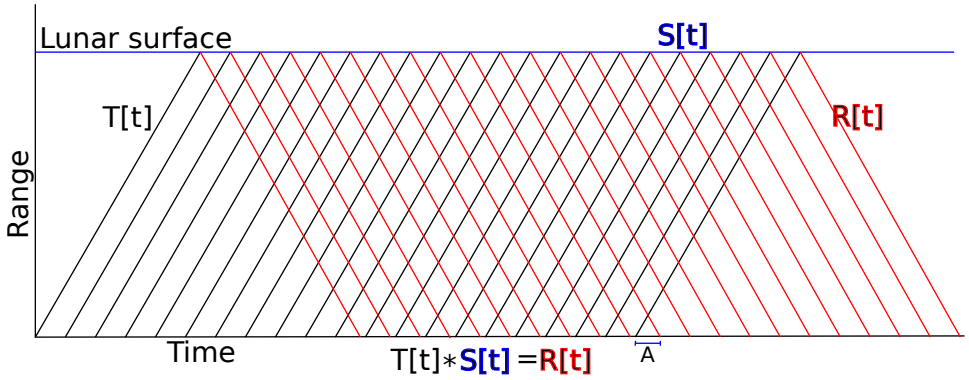

Figure 2.10: Range aliasing and convolution

figure 2.10, a pulse T[t] is sent towards the Moon. This pulse is scattered from the surface which has a system function S[t], then sampled as the returned wave R[t]. Since the light travel time is significantly longer than the IPP, several pulses are transmitted before each pulse is returned, causing range aliasing (shown here as the time A). Observed range is found as the time A times the speed of light C divided by 2. If there are other systems interfering with the signal, these can show up as other horizontal lines or rectangles at some range. In order to ensure that the sampled system is the desired one, the range alias must not coincide with some other known system, such as the ionosphere. The

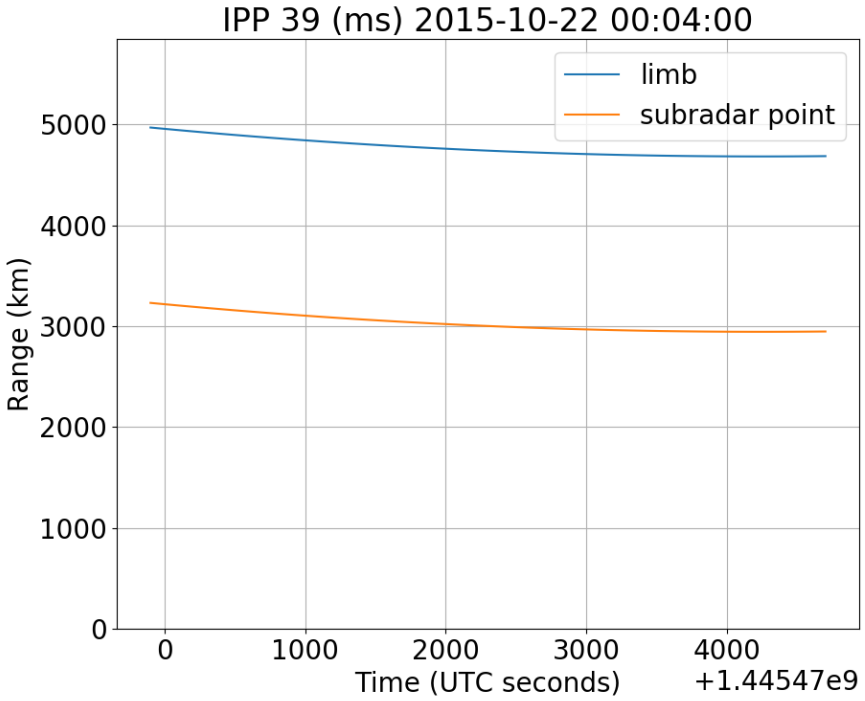

Figure 2.11: This figure shows the movement of the Moon over the course of the experiment with the aliased range in the y-axis. The blue line is the limb, where the lunar surface curves out of view, and the orange line is the sub-radar point. Neither aliases outside our acceptable range during the experiment.

total travel distance in one IPP is 5650 km. The Moon also migrates during the observation period, and one must choose IPPs in such a way as to ensure that it doesn't migrate outside the clear region, see figure 2.11.

2.3.6 Radar resolution

While the theoretical range and frequency resolution would be approximately 2.5 km in the frequency direction and 1.5 km in the range direction, ionospheric distortion and averaging has reduced the effective resolution to 15 km in frequency and 20 km in range [39].

For a visualization of range resolution cells, see figure 2.12. As the surface curves away, the range cells become progressively narrower due to the surface aligning more closely to the radar look direction.

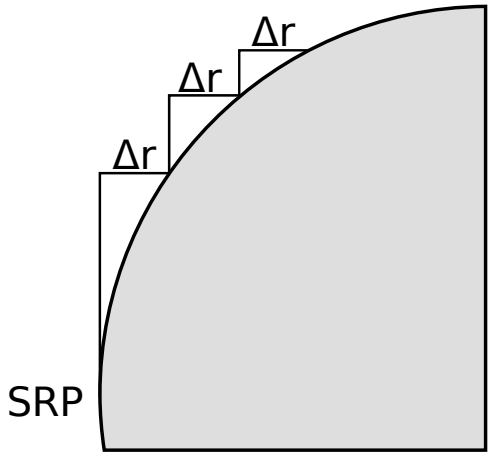

Figure 2.12: As the angle of incidence grows, the circles that make up individual range cells will be a shorter distance apart. This happens because as the surface curves away, the ground becomes more parallel to the incoming radiation. In this figure, this effect is displayed through the use of a constant range increment at different places on the edge of a sphere.

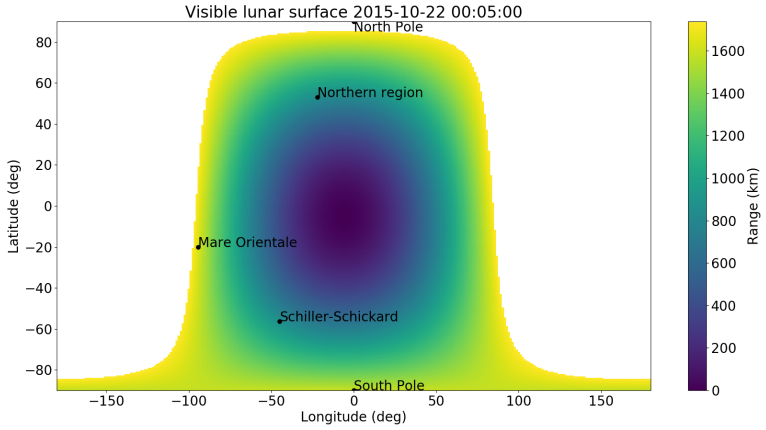

Figure 2.13: This figure shows the range variable across the lunar surface as a function of latitude and longitude. Note that the center is shifted somewhat south and west, so that we can see Mare Orientale as well as the area immediately surrounding the south pole. The north pole is hidden from view because of this. This figure assumes that the Moon is perfectly spherical.

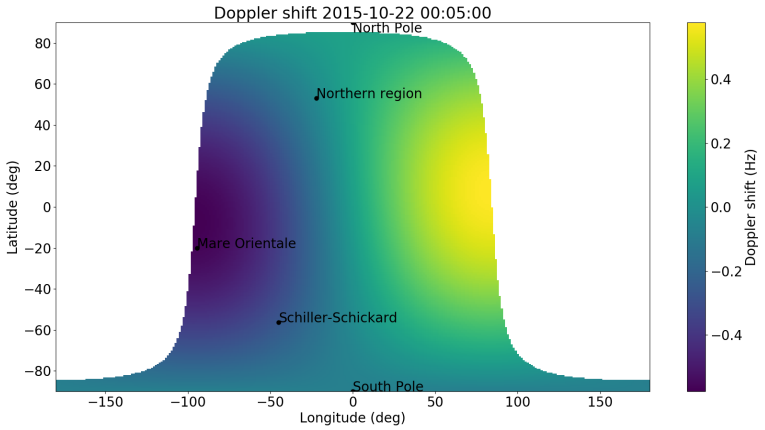

Figure 2.14: This figure shows the Doppler-spread as function of latitude and longitude. Here we can see the slight tilt of the rotation axis in that the east and west Doppler "poles" are shifted slightly north and south in relation to each other. The total Doppler spread is a little over 1 Hz. This figure assumes that the Moon is perfectly spherical.

Figure 2.13 shows the spread of range along the radar line of sight over the lunar nearside. Together with figure 2.14, which shows the Doppler variable across the lunar nearside, one can convert between the range-Doppler representation and a latitude-longitude projection (as in figure 1.3).

The mean and variance of the returned power also carries information. If an area has high variance that might mean that the area contains multiple surface types or has a low signal-to-noise ratio. In addition, if there is a low scatterer population being probed by the wave, small variations in the scatterer density will more severely affect the variance than in high scatterer population areas. In order to determine these properties, one can create histograms of selected areas and compare the width, shape and position of the distribution.

Bragg scattering is a mechanism where periodic variations in the refractive index cause constructive or destructive interference of the returned signal. If the refractive index has random variations, these variations can cause situations where Bragg scatter occurs for small areas, adding a zero mean random variable to the returned signal. Unless there are regular, periodic structures in or on the lunar surface, Bragg scattering should not affect the mean returned power over the entirety of the lunar surface.

3 Method

In this chapter, we will discuss the methods used to investigate what physical properties caused the anomalously low depolarized radar return in the S-Z and F-I regions, which where discussed in the introduction.

We have developed a model for subsurface volume scattering. With the help of this scattering model, we have formulated three hypotheses that could explain low radar reflectivity in the S-Z and F-I regions. We will discuss each hypothesis in detail and discuss what methods can be used to prove or disprove them.

3.1 Scattering model

In order to provide a first order model of subsurface volume scattering, we will introduce a simple sphere packing model. This model includes inclusions of different sizes, and also contains a uniform loss-tangent. As far as we are aware, this is a novel technique for identifying the size categories of scatterers responsible for depolarized return of the lunar surface, although it is possible that others have created similar models before.

Using a simplistic sphere packing model it is possible to investigate what sizes of inclusions contribute to volume scattering. This model assumes that scatters within a volume are independent. By creating simplistic models for the density

of spheres in a volume and the radar cross section of each sphere as a function of their diameter, we can estimate what size of objects contribute most per unit volume to the total depolarized return.

The number of particles of diameter d per unit volume is roughly proportional to $n = d^{-3}$, assuming that the inclusions are evenly distributed in mass. If we express the diameter in units of the wavelength illuminating the objects, there are three different scattering regimes: Rayleigh scattering, resonant scattering and optical scattering. If the objects are irregular, the resonant scattering regime can be approximated with optical scattering. In our simple model, we will only use Rayleigh or optical scattering. For Rayleigh scattering, the radar cross-section (RCS) of each object can be approximated as $\sigma^* = d^6$. In the optical regime, the RCS of each object can be approximated as $\sigma^* = d^2$. In combination, we get an approximation of the total radar cross section of a unit volume as $\sigma_v = n\sigma^*$. In the Rayleigh regime, this leaves us with $\sigma_v = d^3$, where $d < 1$, and in optical we get $\sigma_v = d^{-1}$, where $d \geq 1$. By combining the model for Rayleigh and optical scattering, we can study the radar cross-section per unit volume as a function of object diameter. The volume scattering in highland terrae can be assumed to be caused primarily by scatterers that have a diameter of $0.1\lambda - 1\lambda$.

As seen in figure 3.1, there is a sharp increase in RCS as the diameter of the objects approach 0.2λ, and a more gradual decline as the objects again grow in size. This happens because the number of objects compensates for the reduced RCS per object for diameters just below the radar wavelength, but as d decreases, the RCS decreases much faster than the number of objects in the Rayleigh domain.

3.2 Hypotheses

The primary objective of this study was been to understand why certain regions of the Moon appear radar dark in the 6-meter wavelength polarimetric radar map. We start by formulating several plausible hypotheses and proceed to analyse these potential explanations using other supporting data and modeling. There are several mechanisms that could cause the reduced depolarized echo. The three hypotheseswewill examine and discuss are as follows:

- Hypothesis 1: Lower than average spatial density of wavelength-scale inclusions in regolith

- Hypothesis 2: Higher than average dielectric loss tangent in the regolith in the regions

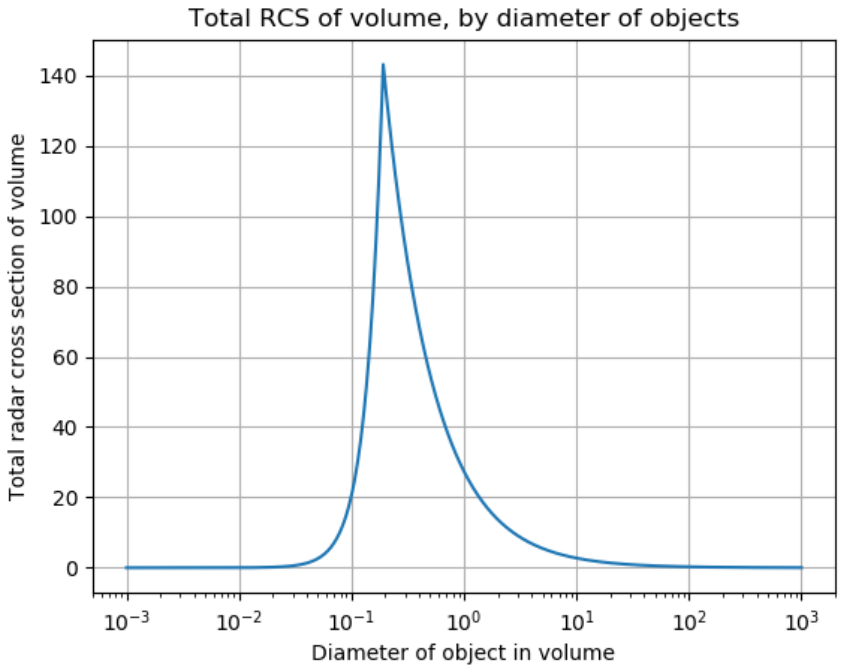

Figure 3.1: A semi-log plot of total radar cross section of a volume of packed objects by the diameter of the objects. Notice that the peak return is for a volume of spheres with diameter near 0.2λ

.

- Hypothesis 3: A substrate with shallow regolith cover

Each of these physical characteristics could explain the observed results, by itself or in any combination, but could be differentiated with supporting datasets and different investigation techniques.

3.2.1 Hypothesis 1: Low scatterer population

The depolarized portion of the returned power is mainly caused by resonant scattering from buried objects. This is because the lunar surface is generally smooth on the wavelength scale, and there are few opportunities for double-bounce surface scattering. If a region has a significant reduction of available scatterers with a diameter in the range of $0.1 - 1.0\lambda$ in the volume probed by the radar, the total depolarized radar cross section would be greatly diminished.

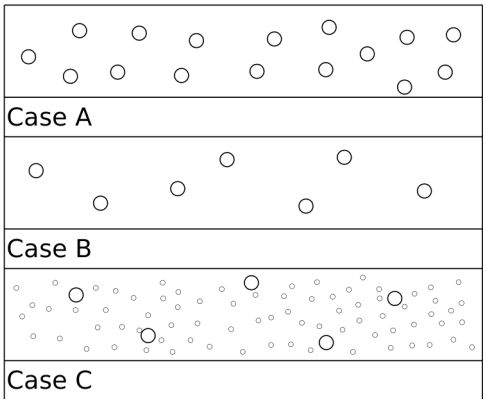

Figure 3.2: Differences in rock population can cause differences in returned depolarized power. Case A: high population of wavelength size scatterers. Case B: low population of wavelength size scatterers. Case C: low population of wavelength size scatterers, but high population of rocks below detection limit.

In figure 3.2, we see three different cases for rock populations in lunar regolith. In A, there is an abundance of rocks that are comparable in size to the radar wavelength, which results in a strong depolarized return from the area due to resonant scattering. In B, there is a low population of rocks in general, leading to lower depolarized return. In C, there is a high population of rocks sufficiently small to be undetectable as well as a low population of wavelength-scale rocks.

This hypothesis could be investigated by examining the returned echo. In a case of low scatterer population, small variations in population can cause significant

variations in returned echo power. In the case of an otherwise homogeneous area with low mean echo power and high variance, this could be explained through a low population of scatterers. Highly populated areas might be entirely saturated with scatterers, due to the radar signal being almost entirely reflected before it can penetrate deep enough to attenuate. Here, variations in the depth of buried scatterers, relative to penetration depth, will have more influence over returned power than variations in scatterer population.

We have also attempted to use model-based polarimetric target decompositions to extract further information from our fully polarimetric dataset. This would have involved using our a-priori knowledge and assumptions about the lunar landscape to categorize which scattering mechanisms would cause certain polarized states to infer regions where the different scattering mechanisms dominated. This work would involve either adapting an already developed decomposition model to the lunar environment or creating a new one from scratch. We determined that a possible solution would be an adapted Freeman-Durden target decomposition scheme where the canopy of cylindrical scatterers in arbitrary orientations is replaced by spheres of variable size and ellipticity. We realized that this work would be outside the scope of this thesis, and abandoned the pursuit.

3.2.2 Hypothesis 2: High dielectric loss

If the chemical composition of the regions are significantly different from otherwise similar areas such that the loss tangent is abnormally high, the radio wave would attenuate faster and have fewer means of scattering favourably back to the receiver. If the regions have higher iron oxide or titanium oxide content than other similar areas, the volume scattering component of the radar return would be lower. In figure 3.3 the effect of an increased loss tangent on the available scatterers in a volume. The same pulse is transmitted into a medium with loss tangents A or B, where A <B. When the penetration depth decreases, the total number of scatterers in a rough medium also decreases, which in turn affects the total depolarized power returned to the antenna. This can cause the effects of a reduced penetration depth to appear similar to the effects of a reduced population of scatterers.

In order to judge the validity of the second hypothesis, we can search for areas with surface chemical compositions similar to the low-return areas. If we can find highland areas with similar surface chemical properties, we can then compare the depolarized radar return. In the case where there is a strong correlation between the surface chemical properties and the depolarized returned power, this will suggest that the areas identified as ”abnormally dark” was misidentified and are actually ”normally dark” for areas with their surface

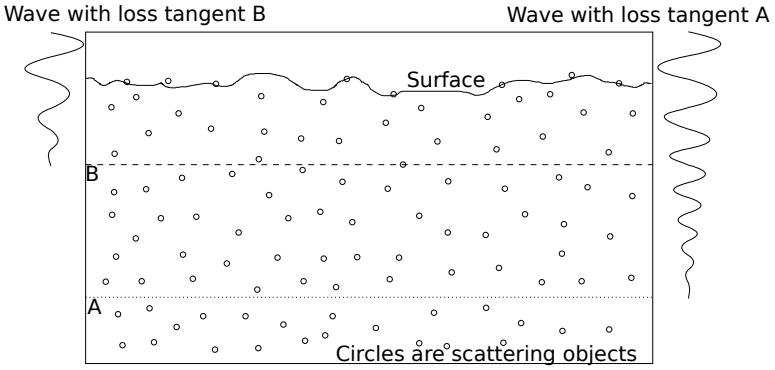

Figure 3.3: An increased loss tangent reduces penetration depth, and thereby reduces the available population of scatterers. The dotted line represents the penetration depth in standard regolith conditions, while the dashed line represents the penetration depth of a high-loss regolith.

chemical properties. In the case where there is no such correlation, it will suggest that attenuation due to surface concentrations of iron and titanium are not enough to explain the loss of power.

Due to the possibility of a difference in the volume chemical composition and the surface chemical composition, there can also be large differences in the loss tangent as the signal propagates through the volume. The depth distribution of lossy chemicals in these regions are, as far as we have been able to determine, unknown. The current methods of measuring the chemical composition of lunar soils are through physical samples and optical studies, which do not penetrate deep enough into the soil to get a comprehensive view.

3.2.3 Hypothesis 3: Buried substrate

If the region has only a shallow regolith over a smooth slab, the volume scattering component is reduced due to the smaller volume to scatter from. This could be confirmed by other datasets, such as the Kaguya lunar sounder. With the LRS instrument it is possible to create images of the subsurface beneath the satellite as it passes over the lunar surface. A deep regolith is expected to have either uniform backscatter in the entire depth, or a backscatter function that depends on the depth beneath the surface. If there is a basaltic substrate, the backscattered power should be much lower in this slab than in regolith, as well as provide a recognizable reflection on the interface between the regolith and the slab. If we can find areas where such a slab is present, we can compare the images of a continuous slab beneath regolith and images of the anomalous areas.

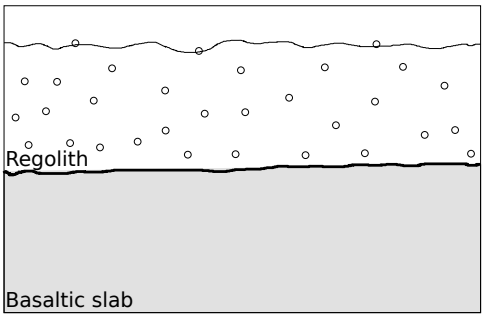

Figure 3.4: If there is a slab of different material beneath the regolith, this will affect the returned power. The shaded area represents a basaltic slab which is internally smooth and has a high loss tangent.

In figure 3.4 there is a slab of basaltic material beneath regolith. This slab has a very low population of volume scatterers and has a significantly higher loss tangent than the regolith covering it. If the regolith covering the slab is shallow enough that the radio signal would normally penetrate into the slab, the lack of scatterers and high loss tangent will mean that the returned power will be lower than would be expected for an area without a shallow basalt slab. The interface between the regolith and the basalt will also reflect a certain amount of power back, but the volume of basalt will be expected to return much less power than regolith, and attenuate the signal at a greater rate.

4

Results and discussion

In this chapter we present the results of our analysis of the three hypotheses introduced in the previous chapter. We will present the results of each hypothesis and discuss them in turn.

In figure 4.1 there is a scattering law measurement scaled by the total projected area available for each resolved range gate as a function of the angle of incidence assuming the Moon is perfectly spherical. The depolarized component is initially about 20dB lower than the polarized component, but decreases less significantly with angle of incidence, resulting in approximately equalizing near the limb. Some of the depolarized power near the subradar point is caused by crosstalk, where polarized power is interpreted as depolarized power by the instrument.

Depolarized power does not depend as much on the angle of incidence as the polarized power, which supports our reasoning that the depolarized radar returns primarily originate from volume scattering events.

4.1 Hypothesis 1: Low scatterer population

In figure 4.2 we see histograms of the radar return of five different areas on the lunar nearside, marked on a cylindrical projection in figure 4.3. As we can see, there is a significant difference in the mean brightness in the F-I

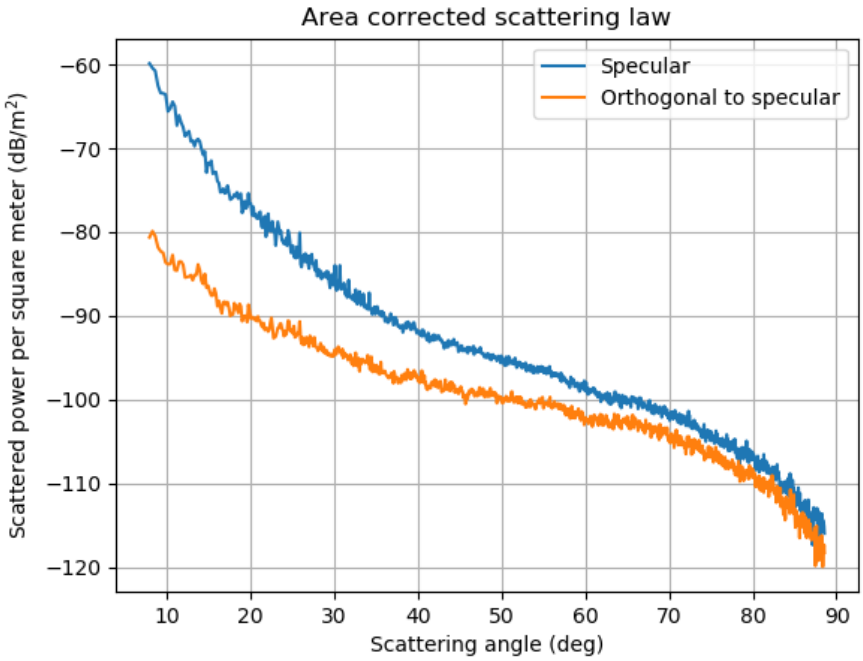

Figure 4.1: Area corrected scattering law measurement from the same radar data as the SAR maps created by Vierinen et al. [39]. Note that both the polarized and depolarized return is dependent upon the angle of incidence, though the depolarized return is less affected. The polarization ratio decreases significantly from the subradar point to the limb. Note that 10 points on both edges were discarded due to noise.

region (figure 4.2 1) and the highland area with a comparable FeO surface content (figure 4.2 2). There is also a large difference in the brightness variance between these areas and the southern hemisphere highland region (figure 4.2 4). The Schiller-Zucchius basin has a lower variance than the northern areas and a lower mean than southern highlands. Oceanus Procellarum (figure 4.2 5) has both low variance and very low mean. This is possibly due to high loss tangent and consistently thin regolith, leading to low penetration depth and low rock variance. This could also be the result of low signal-to-noise ratio, combined with the averaging done when processing the signal. This would cause near-Gaussian noise.

Rock abundance was investigated by Bandfield et al. [1], and the F-I region appears to have a small reduction of rocks which are between 0.5m and 1m in diameter, while the S-Z region appears to have a slightly higher than average rock population. This means that rock scarcity is a possible contributor to the low return in the F-I region, but the increased rock population in the S-Z region would suggest a higher depolarized return if the buried rock population is proportional to the surface rock population. The variations in rock population are small, and we can't be certain that the volume rock population is correlated with the surface rock population. Lunar surface texture is dependent on the age of the surface, where older surfaces will have fewer rocks due to weathering effects. This adds in the difficulty of showing that scatterer population is a significant contributor to the low depolarized return, as surface rock population measurements might form a false view of the buried rock population

Neither area is drastically different from other areas in regards to their visible rock populations. The northern low return region has slightly lower rock concentration than normal for highland areas, while the southern low return region is slightly higher than normal. This, combined with models of lunar subsurface structure, means that it is unlikely that the results can be explained through a lack of scatterers in the region. It is important to note, however, that space weathering and micrometeorite impacts only affect the topmost layer of the lunar soil, and larger impact events are required to reveal and mix deeper layers. This means that for older surfaces that have not recently been excavated by any large impact events, there might not be a correlation between surface rock populations and buried rock populations[27].

4.2 Hypothesis 2: High dielectric loss

Due to our inability to identify the prevalence of iron and titanium in the deeper layers of the lunar surface, we must rely on surface measurements to estimate volume loss tangents. This might cause erroneous conclusions if the

surface layer has a significant difference in chemical composition to the rest of the volume probed by the radar.

In figure 4.4 enhanced-contrast reprojected images of Campbell's 70cm map and LROC images in the same projections. On the left, we see that at 70 cm, the northern terrae region has significantly reduced depolarized backscattered power. Due to the difference in penetration depth, if the reduced echo power is caused by the same mechanism as in the 6 meter map, it must be present in the upper layers of the soil. This could be due to a reduced penetration depth caused by chemical differences or a depletion of rocks in the size range of 7 cm to 600 cm, which would be the predominant source of volume scattering in both maps. This seems unlikely, but we cannot rule it out without more sophisticated measurements. The area is surrounded on three sides by maria, and shows a higher than normal FeO concentration for terrae. If the surface composition is representative of the volume composition, this will cause a reduced penetration depth.

While the radar-dark area has a high surface FeO content, another area further east beyond the mountain range Montes Alpes has a similar surface iron content, but also much higher depolarized radar backscatter, both in 70 cm and 6m. This suggests that there are differences in the volume probed by the radio wave in these areas. The difference could be the volume chemical composition, where the high backscatter region has a thin layer of high iron content on the surface, but a volume composition closer to standard lunar highland soils.

The S-Z area is seen on the right side of figure 4.4. The Schickard crater is visible in the top left of the marked area as a dark blur, and the center of the ancient impact basin is visible in the middle. These areas correspond well to the darkest parts of the same area in figure 1.2, but the darkened halo surrounding the ancient impact basin is not visible. This implies that the halo seen in the 6 meter map is caused by something beyond the reach of the 70 cm wave.

The Kaguya LRS radar instrument probes a volume 10 times deeper than the Jicamarca telescope, assuming no frequency dependence in the loss tangent. This means that the near-surface volume has a smaller effect on the total returned signal. It should also be noted that the LRS only measures one polarization with a low incidence angle, leaving the signal dominated by specular returns from the surface. Despite this, the LRS data will provide useful information about the deeper volume of the lunar crust. It helps indicate how deep the cause of the anomalous depolarized radar return runs by showing whether or not the disturbance also affects the 60 m wavelength returns.

However, the dark area identified in the 6 m map appears similar in all respects

to other highland areas in our maps based on the Kaguya data. We mapped both surface power (see figure 4.5) and subsurface (1000 m) power (see figure 4.6), as well as the ratio between the two (see figure 4.7).

In figure 4.5 we have plotted the surface echo for each latitude and longitude for which there was data. Due to the low incidence angle, the maria have a stronger specular reflection than highlands. Here, the F-I region appear similar to other highland areas. Another noteworthy feature is that surface slopes are not accounted for, leaving dark rings around large impact features, like mare Orientale.

In figure 4.6 we have plotted the returned power from 1000 meters below the surface echo. Few features are visible, and the northern highland area is entirely unremarkable. In the south, the crater Phocylides appears to be very bright. This could possibly be due to echoes from the crater rim folding over the crater floor. If we misidentified a side echo from the crater rim as the surface, echoes from the bottom of the crater could possibly be interpreted as subsurface echoes, distorting the result. As there are few areas with these abnormal bright spots, there is no reason to think that this distortion is widespread, and the effect can be disregarded.

In figure 4.7 we see the ratio of subsurface to surface power. Here, we can see the maria as dark surfaces with the highlands up to 10 dB higher in power. Again, the areas we are investigating appear to not be significantly different from other highland areas to the LRS instrument's 60 m radar.

None of the global plots of LRS data show any significant difference from the radar-dark areas identified by Vierinen et al. [39]. This suggests that the volume probed by the LRS is relatively similar for all the highland regions. One possible reason for this is that the loss tangent formula was empirically determined for a different frequency. If the loss tangent depends significantly on frequency, this could lead to problems when comparing maps made with various wavelengths. To our knowledge, no estimate for the loss tangent of lunar soils at 5 MHz as a function of chemical composition currently exist. If we assume that the loss tangent does not change radically in the span of frequencies we are working with, this suggests two different properties of the medium. The first is that the mechanism which caused the reduction in power does not significantly affect the polarization expected for specular scattering. The other alternative is that the mechanism is most present in the upper layers of the soil. This is because the wavelengths used each penetrate a different volume of the soil. While the 70 cm wave will be dominated by approximately the first 3.5 m, this layer isn't as influential on the 6 m wavelength scale. Rather, the 6 meter wavelength signal will be dominated by the first 30 m. Therefore, changes in the volume are sampled at a different depth with different wavelengths.

4.3 Hypothesis 3: Buried substrate

By using the techniques described by Oshigami et al. [31], we have searched for buried substrates in the northern highlands. We attempted to map the areas with continuous subsurface reflections in both longitude and latitude, but discovered that only a small fraction of the anomalously dark areas contained such signatures. Only near the edges of highland terrae and mare basalts were these structures common. East of the crater Foucault in the eastern edge of the F-I region there was a clear continuation of the basaltic surface beneath a layer of highland material, see figure 4.8.

There are no indications that there is a large buried surface spanning most of the F-I region which could cause the discrepancy in the radar return according to data gathered from the Kaguya lunar sounder instrument. It is also noteworthy that to the 60m Kaguya beam, the area is not notably different from other highland areas. Both the surface echo and subsurface echo power is comparable to other highland regions, suggesting that the deep volume of the region is not significantly different from other highland areas at 5MHz.

We also investigated for buried surfaces in the Schiller-Schickard area, which is claimed by Whitten et al. [41] to be a cryptomare. We were unable to find continuous substrates in the area of reduced depolarized radar return. This indicates that the Kaguya instrument may not be suitable for cryptomare detection. One possibility is that the covering regolith is shallow enough that it becomes hard to distinguish between the surface reflection and the subsurface reflection. The 6 m wavelength SAR map shows a reduced depolarized power return in this area, but this alone is not conclusive, due to the high iron content in the soil in this area.

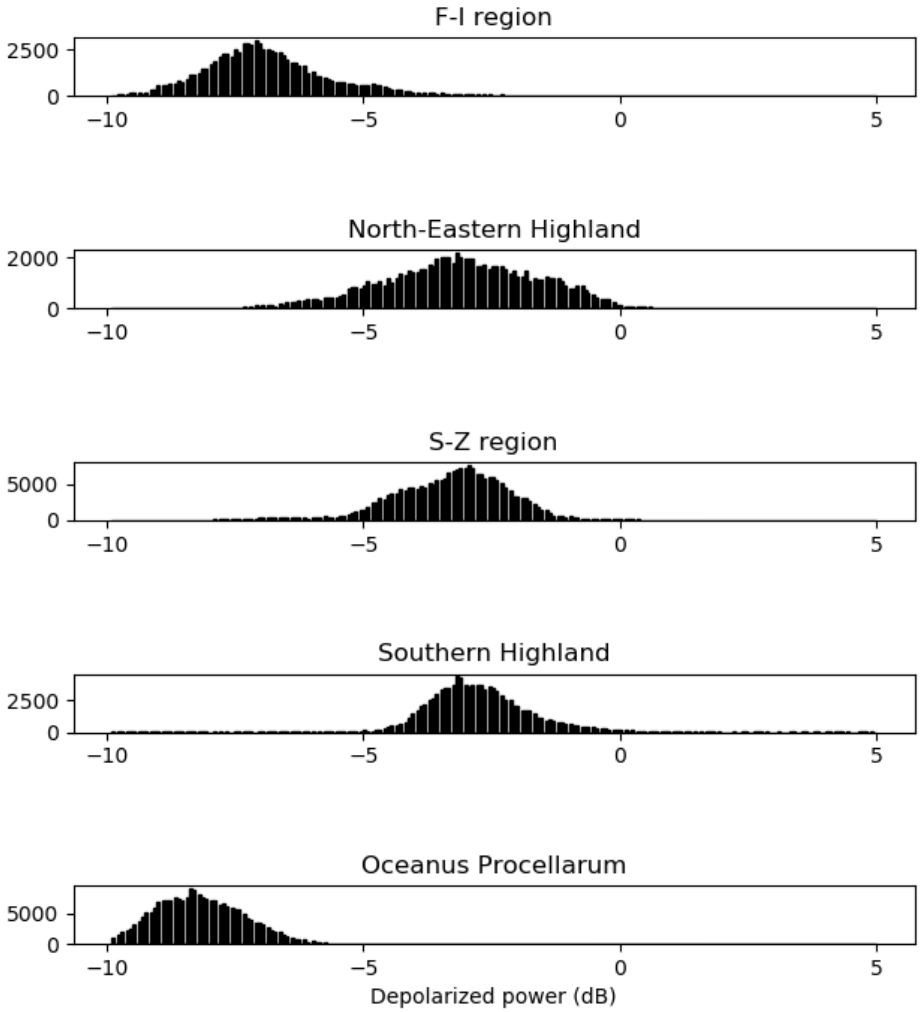

Figure 4.2: This image shows histograms of the depolarized radar return in five selected regions of the Moon. 1: The F-I region, excluding obvious craters and visible mare. 2: Highland area east of Mare Frigoris with comparable Fe-content to 1. 3: S-Z region. 4: Highland area on the southern hemisphere, east of the crater Tycho. 5: mare area in Oceanus Procellarum with very few visible craters.

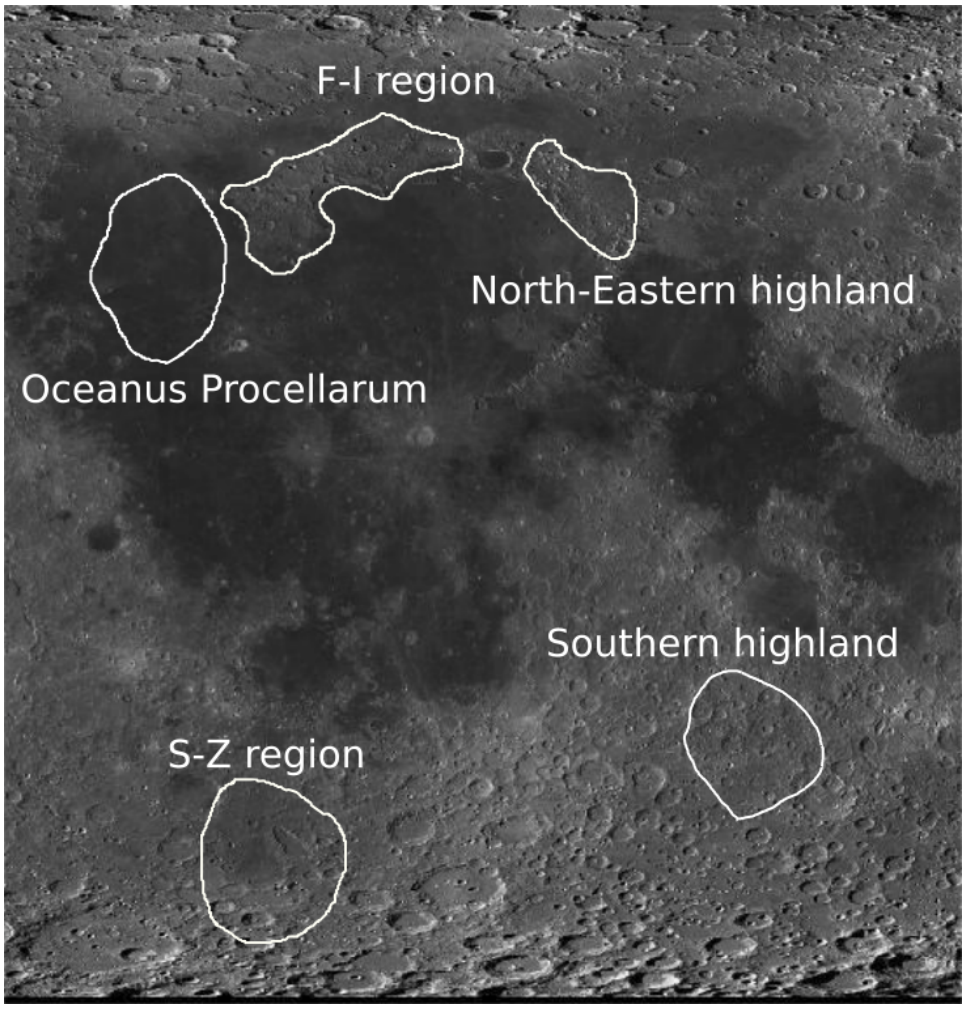

Figure 4.3: This figure shows the approximate locations used to create the histograms in figure 4.2.

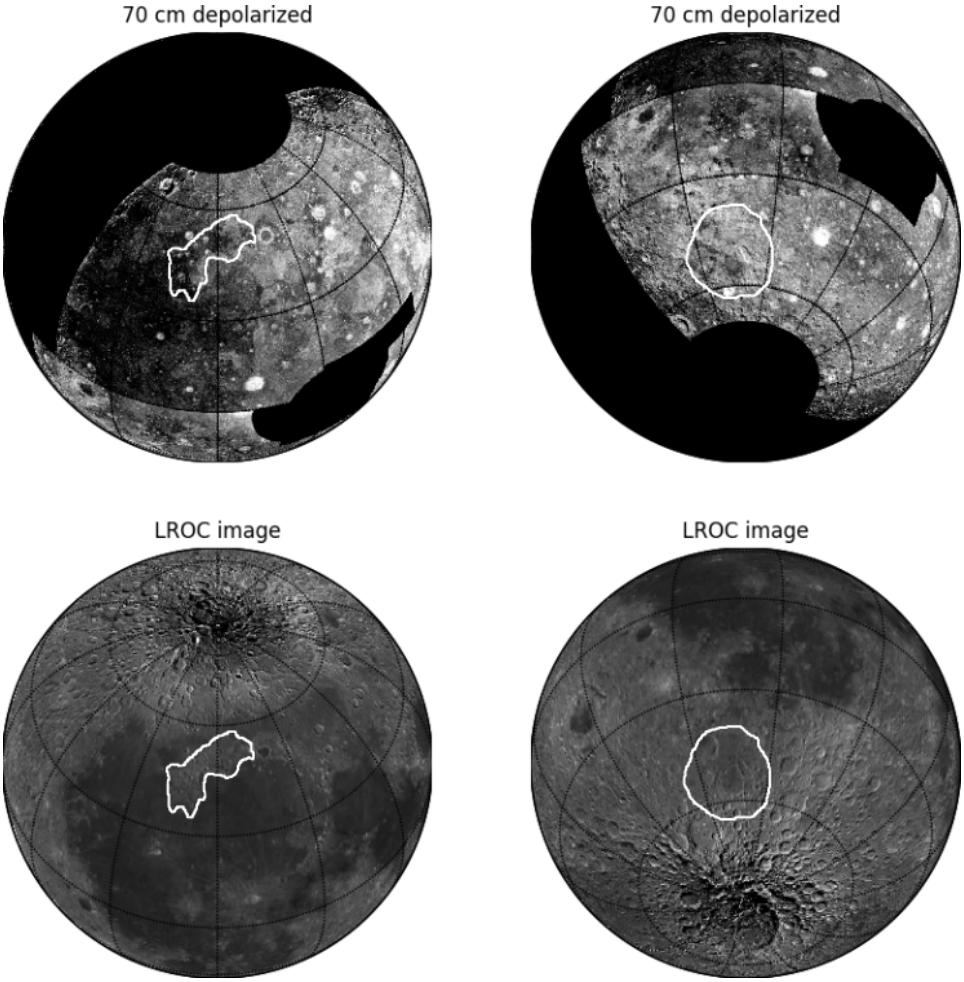

Figure 4.4: This figure shows reprojections of the 70 cm depolarized SAR map made by Campbell et al. [5]. The F-I region is shown in the SAR map in the top left, LROC image on the bottom left. On the right is the S-Z region. 70 cm data from NASA PDS.

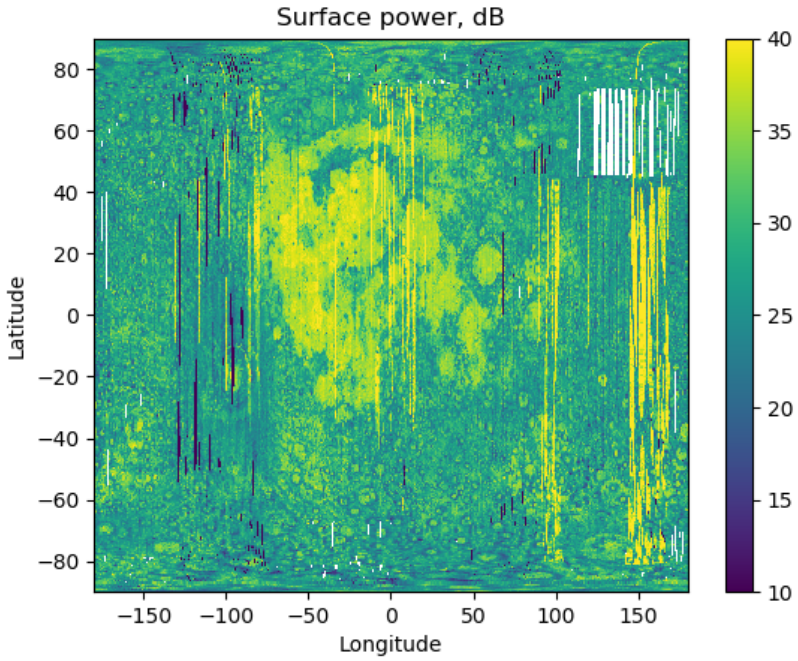

Figure 4.5: Global map of surface echo power gathered by the LRS instrument. Here, the smooth maria show a strong return, while the comparatively rough highlands show returns several decibels lower. Note that the white strips are areas with no data, and the solid blue or yellow lines are possibly caused by errors in the data gathering process.

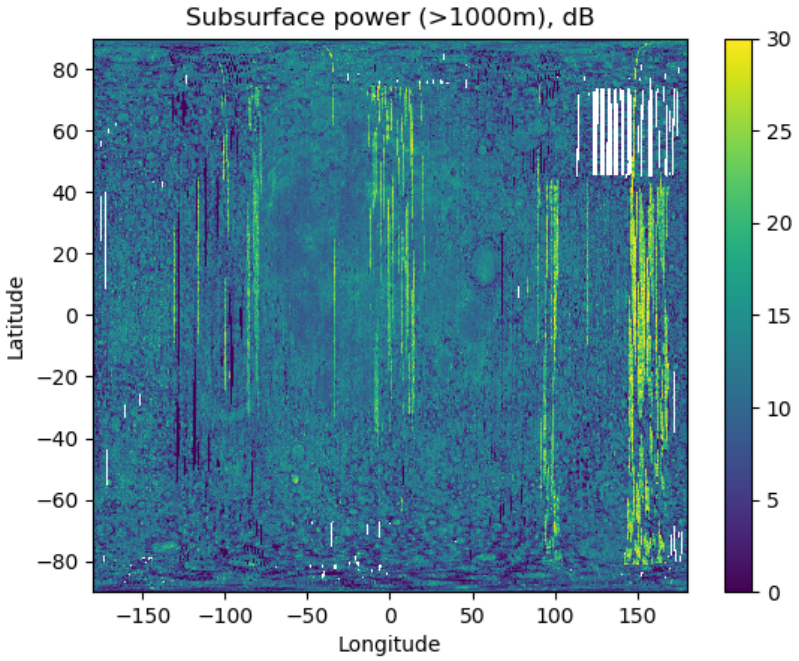

Figure 4.6: Global map of subsurface power, gathered from 1000m below what we found as the surface echo. There is very little to distinguish maria from terrae, and very few features are recognizable.

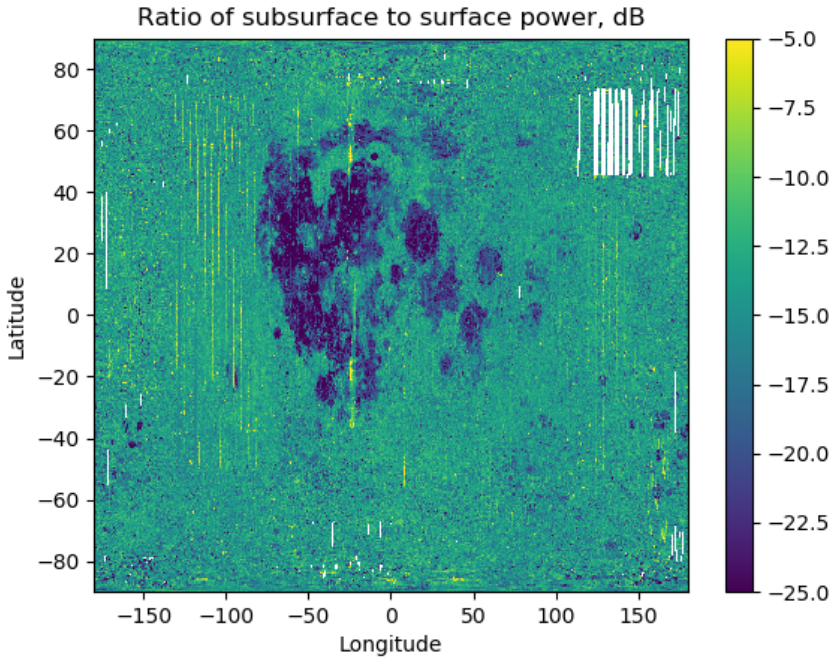

Figure 4.7: This is the ratio of the subsurface power to the surface power. Here, highlands are identified by their significantly higher ratio than maria. Again, there is little difference between the potential cryptomare areas being investigated and other highland areas.

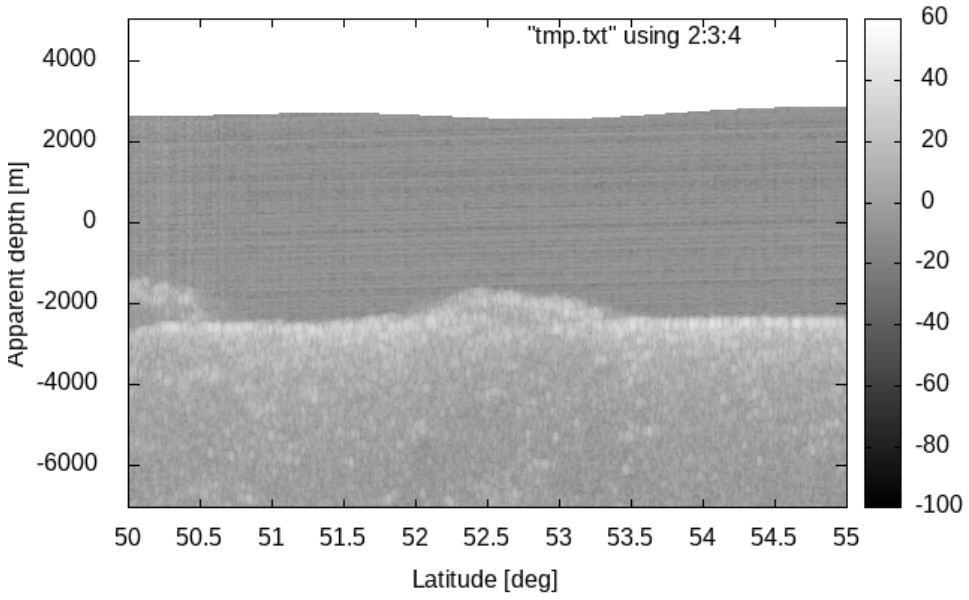

Figure 4.8: The leftmost part of this figure shows a strong, continuous echo from beneath a highland deposit over the south-western edge of Mare Frigoris, near the crater Foucault. This echo is continuous in both latitude and longitude until it is disrupted by the crater, and continues east of the crater.

5

Conclusions

In order to shed more light into the mysteriously low radar return in the M-I and S-Z regions, we have explored a number of other Lunar datasets, including 70 cm polarimetric radar maps, multi-spectral FeO and TiO_2 abundance maps, and LRS 60 meter wavelength radar returns. Each of them provides additional clues to the physical properties of the regions. We have also investigated volume radar scattering with a simple resonant scattering model which we have developed. In this chapter we will seek to interpret our results and determine what our findings mean in the context of the fields of radio remote sensing and lunar volcanic history.

5.1 Our findings

We explored three hypotheses:

- Hypothesis 1: Lower than average spatial density of wavelength-scale inclusions in regolith
- Hypothesis 2: Higher than average dielectric loss tangent in the regolith in the regions
- Hypothesis 3: A substrate with shallow regolith cover

Hypothesis 1 and hypothesis 2 are hard to confirm or disqualify, as both could present very similar results for depolarized radar backscatter. In our comparisons of several datasets of physical properties of the lunar surface in both regions, we have found no direct evidence that there is a significantly diminished population of volume scatterers in either area. Neither have we found a convincing suggestion as to how this would occur in only these areas on the Moon. We therefore conclude that there is no apparent reason to believe that there is a lack of scatterers with diameters spanning the range of 7 cm to 12 m in the entire F-I region, but we can not conclusively rule it out.

We have not found a model based on empirical evidence for the relationship between rock population on the surface and the volume rock population. Despite this, the low variance in surface rock population in large areas lead us to believe that a lack of available volume scatterers is not the cause of the reduced depolarized return.

Hypothesis 3 was considered the most falsifiable, as a continuous subsurface structure should appear on the maps created from the Kaguya LRS data. No such structures were detected, and as such it appears very unlikely that these caused the reduced depolarized power.

Hypothesis 2 then appears to be the most likely cause of the reduced depolarized return, as we were able to detect increased concentrations of lossy chemicals in both regions. The estimates for FeO and TiO_2 concentrations in the Frigoris-Imbrium area are comparable to other regions with significantly higher depolarized returns. Surface concentrations of iron and titanium are not enough to explain the reduced power in this area, and some other factor must be introduced in order to explain these results. It could be an increase in the subsurface concentration of loss-causing chemicals, but we cannot say for certain.

If the Frigoris-Imbrium highland area was an ancient basaltic deposit that appeared while the cratering rate was still sufficiently high to break apart surface structures, the low return could be caused by the increased iron and titanium content of broken basalts being mixed with ejecta from highland areas surrounding it. The basaltic gravel was then buried by ejecta from large impacts in the surrounding area, like the impact which formed the Imbrium basin. Later, the cratering rate reduced, and volcanic flow complexes were no longer shattered, and the maria surrounding the area formed. This would cause the deeper crustal layers to have a higher loss tangent than otherwise similar highland areas, thus explaining the reduced power.

While investigating our main scientific question we also found an area near the craters Harpalus and Foucault that displayed interesting qualities (see figure

4.8). This area is a mound of highland material which appears to have been connected to the main highland region south of Mare Frigoris. This mound appears to have a subsurface reflection that is a continuation of the Mare Frigoris basalt plain. This may indicate that this mound was supplanted on Mare Frigoris after the event that led to it's formation. This appears to be either a distal or proximal ejecta type cryptomare. We have not identified which impact could have provided the material that makes up this mound, making it hard to determine it's classification. While we cannot say that the surface reflecting the Kaguya signal must be basalt, it appears to have similar qualities as the exposed mare surface when interacting with the 60 m wave. We therefore posit that this is a cryptomare formation.

5.2 Suggestions for further work

In order to conclusively determine the cause of the deviating results found both in the JRO study and the 70-cm map by Campbell, modelling of the subsurface rock distribution, both in size, quantity, and chemical composition should be done. One method of achieving such a task would be large-scale mining operations to uncover each layer of the lunar subsurface (see figure 2.2) and empirically determine a size distribution of buried lunar rocks. This is obviously impractical and massively expensive, and so alternative methods of inquiry are required.

Model-based target decomposition could help ascertain the various scattering mechanisms that dominate the different areas and terrains of the lunar surface. We attempted this, but we ran out of time. If a model of a volume with randomly oriented elliptical inclusions could be created, we might be able to use this to see which scattering mechanisms or characteristics change in the Frigoris-Imbrium highland, and from this further specify what the physical characteristics of the volume would be to provide the observed results. Anne Virkki worked with models that might be applicable [40], but we were not aware of this fact untill very late in the working process.

Computer modelling can also assist in predicting the physical conditions that would lead to similar results. If a detailed computer model that incorporated the various environmental variables in the lunar landscape (e. g. loss tangent distribution by depth, scatterer population and characteristics like size and ellipticity, surface roughness, dielectric properties such as permittivity and permeability, etc.) were created, one could investigate which set of lunar crustal conditions produce similar effects with full-wave simulations to model the scattering of 6 m wavelength radar waves. The results of such simulations could then help direct future research.

Another important model which would help significantly in future interpretations and maps of the lunar surface is a more comprehensive model for the loss tangent of lunar materials. While the samples returned from the Apollo missions have been used to create an empiric model for the loss tangent at 450 MHz, it would be useful to expand the range of frequencies for which this model of the loss tangent of lunar surface materials based on chemical composition is valid.

It would also be advantageous to acquire a larger spread in the frequencies used to investigate the volume. Due to the fact that each frequency will probe a different volume and particle size distribution, this can be used to investigate the thickness of the anomalous layers or which particle size distribution is present in the volume. Due to the difficulty of penetrating the ionosphere at frequencies lower than 50 MHz, expanding into lower frequencies would require more satellite missions. It would then be advantageous to make the satellites capable of transmitting and receiving in two orthogonal polarizations such that the data is usable for polarimetric analysis, like model-based decomposition.

Bibliography

[1] Joshua L Bandfield, Rebecca R Ghent, Ashwin R Vasavada, David A Paige, Samuel J Lawrence, and Mark S Robinson. Lunar surface rock abundance and regolith fines temperatures derived from lro diviner radiometer data. *Journal of Geophysical Research: Planets*, 116(E12), 2011.

[2] Robin Biesbroek and Guy Janin. Ways to the moon. *ESA bulletin*, 103:92–99, 2000.

[3] David T Blewett, BRAY Hawke, Paul G Lucey, G Jeffrey Taylor, Ralf Jaumann, and Paul D Spudis. Remote sensing and geologic studies of the schiller-schickard region of the moon. *Journal of Geophysical Research: Planets*, 100(E8):16959–16977, 1995.

[4] Bruce A Campbell. *Radar remote sensing of planetary surfaces*. Cambridge University Press, 2002.

[5] Bruce A Campbell, Donald B Campbell, Jean-Luc Margot, Rebecca R Ghent, Michael Nolan, John Chandler, Lynn M Carter, and Nicholas JS Stacy. Focused 70-cm wavelength radar mapping of the moon. *IEEE transactions on Geoscience and Remote Sensing*, 45(12):4032–4042, 2007.

[6] Robin M Canup and Kevin Righter. *Origin of the Earth and Moon*, volume 30. University of Arizona Press, 2000.

[7] RL Carpenter. Symposium on radar and radiometric observations of venus during the 1962 conjunction: Study of venus by cw radar. *The Astronomical Journal*, 69:2, 1964.

[8] Leo Depuydt. *Civil calendar and Lunar calendar in Ancient Egypt*, volume 77. Peeters Publishers, 1997.

[9] John V Evans and Tor Hagfors. Radar astronomy. *New York: McGraw-Hill, 1968, edited by Evans, John V.; Hagfors, Tor*, 1968.

[10] Galileo Galilei. *Sidereus Nuncius, or the sidereal messenger*. University of Chicago Press, 2016.

[11] Benjamin T Greenhagen, Paul G Lucey, Michael B Wyatt, Timothy D Glotch, Carlton C Allen, Jessica A Arnold, Joshua L Bandfield, Neil E Bowles, Kerri L Donaldson Hanna, Paul O Hayne, et al. Global silicate mineralogy of the moon from the diviner lunar radiometer. *Science*, 329(5998):1507–1509, 2010.

[12] T Hagfors, JL Green, and A Guillen. Determination of the albedo of the moon at a wavelength of 6 in. *The Astronomical Journal*, 74:1214, 1969.

[13] Tor Hagfors. Some properties of radio waves reflected from the moon and their relation to the lunar surface. *Journal of Geophysical Research*, 66(3):777–785, 1961.

[14] William K Hartmann. Moons and planets. *Belmont, CA, Wadsworth Publishing Co., 1983, 526 p.*, 1983.

[15] William K Hartmann, Cathy Quantin, and Nicolas Mangold. Possible long-term decline in impact rates: 2. lunar impact-melt data regarding impact history. *Icarus*, 186(1):11–23, 2007.

[16] William K Hartmann and Craig A Wood. Moon: Origin and evolution of multi-ring basins. *The Moon*, 3(1):3–78, 1971.

[17] WK Hartmann. Dropping stones in magma oceans-effects of early lunar cratering. In *Lunar highlands crust*, pages 155–171, 1980.

[18] James W Head III and Lionel Wilson. Lunar mare volcanism: Stratigraphy, eruption conditions, and the evolution of secondary crusts. *Geochimica et Cosmochimica Acta*, 56(6):2155–2175, 1992.

[19] Essam Heggy, Paul A Rosen, Richard Beatty, Tony Freeman, and Young Gim. Orbiting arid subsurface and ice sheet sounder (oasis): Exploring desert aquifers and polar ice sheets and their role in current and paleo-climate evolution. In *2013 IEEE International Geoscience and Remote Sensing Symposium-IGARSS*, pages 3483–3486. IEEE, 2013.

[20] Grant H Heiken, David T Vaniman, and Bevan M French. Lunar sourcebook-a user's guide to the moon. *Research supported by NASA,. Cambridge, England, Cambridge University Press, 1991, 753 p. No individual items are abstracted in this volume.*, 1991.

[21] DC Humm, M Tschimmel, SM Brylow, Prasun Mahanti, TN Tran, SE Braden, S Wiseman, J Danton, EM Eliason, and MS Robinson. Flight calibration of the lroc narrow angle camera. *Space Science Reviews*, 200(1-4):431–473, 2016.

[22] R Jordan, G Picardi, J Plaut, K Wheeler, D Kirchner, A Safaeinili, W Johnson, R Seu, D Calabrese, E Zampolini, et al. The mars express marsis sounder instrument. *Planetary and Space Science*, 57(14-15):1975–1986, 2009.

[23] WK Klemperer. Angular scattering law for the moon at 6-meter wavelength. *Journal of Geophysical Research*, 70(15):3798–3800, 1965.

[24] Paul G Lucey, David T Blewett, and B Ray Hawke. Mapping the feo and tio2 content of the lunar surface with multispectral imagery. *Journal of Geophysical Research: Planets*, 103(E2):3679–3699, 1998.

[25] Prasun Mahanti, DC Humm, MS Robinson, AK Boyd, R Stelling, H Sato, BW Denevi, SE Braden, E Bowman-Cisneros, SM Brylow, et al. Inflight calibration of the lunar reconnaissance orbiter camera wide angle camera. *Space Science Reviews*, 200(1-4):393–430, 2016.

[26] AS McEwen and MS Robinson. Mapping of the moon by clementine. *Advances in Space Research*, 19(10):1523–1533, 1997.

[27] DS McKay, RM Fruland, and GH Heiken. Grain size and the evolution of lunar soils. In *Lunar and Planetary Science Conference Proceedings*, volume 5, pages 887–906, 1974.

[28] Jack Mofenson. Radar echoes from the moon. *Electronics*, 19(4):92–98, 1946.

[29] Engineering National Academies of Sciences, Medicine, et al. *A Strategy for Active Remote Sensing Amid Increased Demand for Radio Spectrum*. National Academies Press, 2015.

[30] T Ono, A Kumamoto, Y Kasahara, Y Yamaguchi, A Yamaji, T Kobayashi, S Oshigami, H Nakagawa, Y Goto, K Hashimoto, et al. The lunar radar sounder (lrs) onboard theákaguya (selene) spacecraft. *Space Science Reviews*, 154(1-4):145–192, 2010.

[31] Shoko Oshigami, Yasushi Yamaguchi, Atsushi Yamaji, Takayuki Ono, Atsushi Kumamoto, Takao Kobayashi, and Hiromu Nakagawa. Distribution of the subsurface reflectors of the western nearside maria observed from

kaguya with lunar radar sounder. *Geophysical Research Letters*, 36(18), 2009.

[32] MS Robinson, SM Brylow, M Tschimmel, D Humm, SJ Lawrence, PC Thomas, BW Denevi, E Bowman-Cisneros, J Zerr, MA Ravine, et al. Lunar reconnaissance orbiter camera (lroc) instrument overview. *Space science reviews*, 150(1-4):81–124, 2010.

[33] AEE Rogers and RP Ingalls. Venus: Mapping the surface reflectivity by radar interferometry. *Science*, 165(3895):797–799, 1969.

[34] Hiroyuki Sato, Mark S Robinson, Samuel J Lawrence, Brett W Denevi, Bruce Hapke, Bradley L Jolliff, and Harald Hiesinger. Lunar mare tio2 abundances estimated from uv/vis reflectance. *Icarus*, 296:216–238, 2017.

[35] EJ Speyerer, RV Wagner, Mark Robinson, DC Humm, K Becker, J Anderson, and P Thomas. In-flight geometric calibration of the lunar reconnaissance orbiter camera. In *22nd Congress of the International Society for Photogrammetry and Remote Sensing, ISPRS 2012*, pages 511–516. International Society for Photogrammetry and Remote Sensing, 2012.

[36] PD Spudis, DBJ Bussey, SM Baloga, JTS Cahill, LS Glaze, GW Patterson, RK Raney, TW Thompson, BJ Thomson, and EA Ustinov. Evidence for water ice on the moon: Results for anomalous polar craters from the lro mini-rf imaging radar. *Journal of Geophysical Research: Planets*, 118(10):2016–2029, 2013.

[37] Kentaro Terada, Mahesh Anand, Anna K Sokol, Addi Bischoff, and Yuji Sano. Cryptomare magmatism 4.35 gyr ago recorded in lunar meteorite kalahari 009. *Nature*, 450(7171):849, 2007.

[38] Utdanningsdirektoratet. Læreplan i naturfag (nat1-03). `https://www.udir.no/kl06/NAT1-03/Hele/Kompetansemaal/kompetansemaetter-vg1-%E2%80%93-studieforberedende-utdanningsprogram`, 2013. [Online; accessed 31-May-2019].

[39] Juha Vierinen, Torbjørn Tveito, Björn Gustavsson, Saiveena Kesaraju, and Marco Milla. Radar images of the moon at 6-meter wavelength. *Icarus*, 297:179–188, 2017.

[40] Anne Virkki et al. Planetary surface characterization by modeling radar scattering. 2016.

[41] Jennifer L Whitten and James W Head. Lunar cryptomaria: Physical char-

acteristics, distribution, and implications for ancient volcanism. *Icarus*, 247:150–171, 2015.

[42] Terri Windling. The symbolism of rabbits and hares. *The Journal ofMythic Arts*, 9, 2007.

[43] Charles Wood. Imbrium's eyebrow. *Sky and Telescope*, 136(6), 2018.

[44] Ian Woodward. *The werewolf delusion*. Paddington Press, 1979.

[45] Yang Zuosheng, KO Emery, and Xui Yuix. Historical development and use of thousand-year-old tide-prediction tables. *Limnology and Oceanography*, 34(5):953–957, 1989.